

Award Number:  
W81XWH-07-1-0325

TITLE:  
Multiplex Quantitative Histologic Analysis of Human Breast Cancer Cell Signaling and Cell Fate

PRINCIPAL INVESTIGATOR:  
William M. F. Lee  
Badrinath Roysam

CONTRACTING ORGANIZATION:  
University of Pennsylvania  
Philadelphia, PA 19104

REPORT DATE:  
May 2010

TYPE OF REPORT:  
Final

PREPARED FOR: U.S. Army Medical Research and Materiel Command  
Fort Detrick, Maryland 21702-5012

DISTRIBUTION STATEMENT: (Check one)

☒ Approved for public release; distribution unlimited

☐ Distribution limited to U.S. Government agencies only;  
report contains proprietary information

The views, opinions and/or findings contained in this report are those of the author(s) and should not be construed as an official Department of the Army position, policy or decision unless so designated by other documentation.

<b>REPORT DOCUMENTATION PAGE</b>			Form Approved OMB No. 074-0188	
Public reporting burden for this collection of information is estimated to average 1 hour per response, including the time for reviewing instructions, searching existing data sources, gathering and maintaining the data needed, and completing and reviewing this collection of information. Send comments regarding this burden estimate or any other aspect of this collection of information, including suggestions for reducing this burden to Washington Headquarters Services, Directorate for Information Operations and Reports, 1215 Jefferson Davis Highway, Suite 1204, Arlington, VA 22202-4302, and to the Office of Management and Budget, Paperwork Reduction Project (0704-0188), Washington, DC 20503				
<b>1. AGENCY USE ONLY (Leave blank)</b>		<b>2. REPORT DATE</b> 31-MAY-2010	<b>3. REPORT TYPE AND DATES COVERED</b> Final - 1 MAY 2007 - 30 APR 2010	
<b>4. TITLE AND SUBTITLE</b> Multiplex Quantitative Histologic Analysis of Human Breast Cancer Cell Signaling Cell Signaling and Cell Fate			<b>5. FUNDING NUMBERS</b> W81XWH-07-1-0325	
<b>6. AUTHOR(S)</b> William Lee and Badrinath Roysam  Email: leemingf@mail.med.upenn.edu				
<b>7. PERFORMING ORGANIZATION NAME(S) AND ADDRESS(ES)</b> University of Pennsylvania Philadelphia, PA 19104			<b>8. PERFORMING ORGANIZATION REPORT NUMBER</b>	
<b>9. SPONSORING / MONITORING AGENCY NAME(S) AND ADDRESS(ES)</b> U.S. Army Medical Research and Materiel Command Fort Detrick, Maryland 21702-5012			<b>10. SPONSORING / MONITORING AGENCY REPORT NUMBER</b>	
<b>11. SUPPLEMENTARY NOTES</b>				
<b>12a. DISTRIBUTION / AVAILABILITY STATEMENT</b> Approved for Public Release; Distribution Unlimited			<b>12b. DISTRIBUTION CODE</b>	
<b>13. ABSTRACT (Maximum 200 Words)</b> Many molecular events and cellular processes are preserved in fixed human tumor specimens, and access to this information awaits a method for them to be quantified and analyzed. Hormone receptors, HER2, cell signaling and proliferation events are prognostically and therapeutically important in human breast cancer and can be revealed by immunohistological staining. A novel platform for study of immunostained breast cancer specimens is being developed that will quantify analyte antigens on a cellular basis, i.e. cytometrically. The platform uses multispectral microscopy to examine breast cancer specimens that have been immunostained for multiple cell type and analyte antigens using different chromogens and fluorophores. Multispectral microscopy and spectral separation permits staining for individual antigens to be distinguished and separated from staining for other antigens in multiplex-stained slides. Stains for structural and cell type antigens (e.g. nuclei, epithelial cytokeratins, E-cadherin) are used by FARSIGHT software to segment individual nuclei and cells in images and to identify those that are breast cancer cells. Stains for biomarkers and cell signaling antigens (e.g. ER, PR, HER2, Ki67, p-ERK, p-AKT) are then associated with the segmented cells to quantify expression of these analytes in breast cancer cells on a per-cell basis. Progress in the past year has developed the cell segmentation function of FARSIGHT software so that nuclear (ER, PR, Ki67, p-ERK, p-AKT) and cytosolic/cell membrane analytes (HER2, p-ERK, p-AKT, p-S6) can be cytometrically quantified and their subcellular distribution determined in human breast cancer specimens. FARSIGHT is ready to deploy for histopathological studies in support of clinical trials				
<b>14. SUBJECT TERMS</b> Breast cancer, cell signaling, cell proliferation, histology, image analysis			<b>15. NUMBER OF PAGES</b> - 51	
			<b>16. PRICE CODE</b>	
<b>17. SECURITY CLASSIFICATION OF REPORT</b> Unclassified	<b>18. SECURITY CLASSIFICATION OF THIS PAGE</b> Unclassified	<b>19. SECURITY CLASSIFICATION OF ABSTRACT</b> Unclassified	<b>20. LIMITATION OF ABSTRACT</b> Unlimited	

Table of Contents

Introduction..... 4

Body..... 6

Key Research Accomplishments..... 5

Reportable Outcomes..... 5

Conclusions..... 6

References..... 6

**Principal Investigator:** Lee, William M. F.

**Proposal Title:** **Multiplex Quantitative Histologic Analysis of Human Breast Cancer Cell Signaling and Cell Fate**

### **Introduction**

The objective of this proposal was to build an advanced platform for immunohistological study of breast cancer specimens that retrieves multiplex quantitative molecular information on a cellular basis. Three components make up this platform: (1) Multiplex tissue immunostaining protocols for revealing structural, cell-type and analyte antigens in the same histologic section (the first two types of antigens are to help segment and classify cells, and the last type of antigen is to reveal biological processes/events and prognostic/predictive biomarkers of interest); (2) imaging by multispectral microscopy to capture the information revealed by individual stains in multiplex combinations; and (3) software (FARSIGHT) for automated multispectral image analysis that (i) segments individual nuclei and cells in images, (ii) classifies the segmented nuclei/cells into cell types of interest based on their association with structural/cell-type antigen staining and spatial/ textural features, and (iii) quantifies analyte expression on a cellular basis by associating analyte staining with the segmented nuclei/cells. Operation of the platform was developed using human breast cancer specimens with the goal of quantifying cytometrically antigen staining of known prognostic/predictive value (ER, PR, HER2) or reporting biological events and processes (Ki67, p-ERK, p-AKT, p-S6) relevant to molecularly targeted therapeutic agents.

This project has been in no-cost extension for the past year.

### ***Task 1. Develop robust protocols for multiplex immunostaining of human breast cancer specimens***

We have developed robust immunostaining protocols for detecting analyte antigens in paraffin-embedded human breast cancer specimens that report on cell signaling events (p-ERK, p-AKT, p-STAT3, p-S6), cell fate decisions (Ki-67) and biomarkers of prognostic and predictive value (ER, PR, HER2). Immunohistochemical (IHC) staining for these analytes using chromogenic substrates (DAB, diaminobenzidine) consistently yielded the highest percentage of positive tumor cells (with low background staining). Staining using fluorescent reporters yielded comparable results for some of the analytes (p-ERK, Ki-67, HER2), making immunofluorescent (IF) staining an option when studying these analytes. For other analytes (e.g. p-AKT, p-STAT3), however, IF staining yielded far fewer positive cells, indicating that IF was significantly less sensitive than IHC for studying these analytes. Structural and cell-type antigens (epithelial cytokeratin, CK, E-cadherin, HER2) used for typing segmented nuclei and cells as breast carcinoma cells are generally abundant and equally well revealed by IHC or by IF immunostaining. Putting these individual antigen stains together in multiplex immunostaining protocols, we use IHC staining for the single analyte stained on a slide (employing DAB chromogen) followed by IF staining for the structural/cell-type antigens on the slide. The exception is when HER2 is our analyte, in which case we use IF staining for both HER2 analyte and CK cell-type/structural antigen. To prevent nonspecific staining by the secondary anti-mouse Ig antibodies used in subsequent IF staining (due to cross-binding to mouse antibodies applied previously during analyte IHC staining), we “strip” off all antibodies following DAB staining by incubating slides in a 5% SDS solution at 50°C for 5 minutes. If two analytes are to be studied in the same tumor slide (e.g. p-ERK+Ki67 or ER+PR), we perform dual analyte IHC staining using DAB as the reporter for one analyte and SG Blue as the reporter for the other analyte. We stain for cell-type/structural antigens following completion of IHC analyte immunostaining. We found that staining for phospho-epitopes (p-ERK, p-AKT, p-STAT3) diminish in cut tumor sections a month after sectioning. We have made it a policy to immunostain slides for phosphopeptide analytes within two weeks of sectioning.

### ***Task 2. Optimize multispectral imaging and data capture for subsequent computational analysis***

We have tested various image capture conditions and parameters to determine the optimal for acquiring images for accurate analyte quantification and for adequate sampling of breast cancer specimens. Imaging is performed using multispectral imagers sold by Cambridge Research Instrumentation (CRi, Woburn, MA). Attached to an epifluorescence microscope, these capture photons from 420nm-720nm wavelength in both brightfield and fluorescent modes to record chromogen and fluorochrome staining in brightfield and fluorescent “data cubes”, respectively. We image at 400X magnification, which usually acquires 150-300 breast cancer cells for analysis in each image. We usually acquire 10 images from each specimen, so 1500-3000 tumor cells are analyzed. In the last year of this project, we began to use the Vectra Multispectral Imaging System (CRi) which includes a multispectral microscope equipped with a robotic slide loader and a computer-controlled stage. It includes Inform software (CRi) which allows automated image acquisition at 200X magnification selected from regions of interest (ROI) determined at 40X magnification. The software has the ability to identify regions of breast carcinoma cells in hematoxylin-stained images, and this is used to select the ROI at

low magnification for sampling at higher magnification. We will incorporate this imaging system into our analysis platform as it offers the potential to type cells as breast carcinoma cells without immunostaining. Following image acquisition, Nuance software (CRi) “unmixes” the image data cubes into component stains (“channels”) using the pure spectra of the individual component stains. Currently, we can separate staining by two chromogens and up to five fluorochromes in the same space into distinct channels.

### ***Task 3. Develop computational algorithms for multispectral immunohistological image analysis***

FARSIGHT software was developed to quantify intrinsic and associative parameters associated with cells segmented from multispectral image data. Starting with multispectral images of multiplexed immunostained slides that have been unmixed into individual stain channels as described above, the software is able to quantify key breast cancer molecular biomarkers (ER, PR, Ki67, and HER2/neu) on a cell-by-cell basis. Initially, each nucleus in an image is segmented using data in the hematoxylin (or DAPI) channel. Cell identification/enumeration and all subsequent steps in cytometric analysis depend on accurate nuclear segmentation, and Publication #1 (*Trans. Biomed. Eng.* 57;841-852 [2010]) describes development of our approach for obtaining accurate nuclear segmentation. Subsequent to nuclear segmentation, whole tumor cells are segmented based on the delineated nuclei, and cells classified into cell-types of interest based on their association with immunostaining for cell-type antigens. The intra-cellular distribution of molecular biomarkers and/or analytes is then determined for the cell types of interest and quantified for each cell. Publication #2 (*Histopathology* – accepted with revisions) details the development of FARSIGHT for whole cell segmentation, cell classification and analyte association. Farsight is currently being developed to analyze many images at a time without human intervention/input (batch image processing).

### ***Task 4. Validate immunohistological analysis system and data obtained***

With FARSIGHT developed for segmenting nuclei and whole breast cancer cells in appropriately stained histological images and able to quantify ER, PR and HER2 expression, we are in the process of comparing FARSIGHT quantification of these biomarkers in breast cancer specimens with quantification performed by expert pathologists (validation studies).

Please note that FARSIGHT software has been made freely available for use by the scientific community and is not patented.

### **Key Research Accomplishments**

We have developed robust tissue immunostaining protocols that allow breast cancer specimens to be stained for various biomarkers and biological analytes using DAB chromogen along with histochemical staining for nuclei (with hematoxylin) and immunostaining for cytosol (CK) and plasma membrane (E-Cad) by fluorescence.

We have optimized multispectral image capture of specimens immunostained for multiple antigens and structures such that staining for each is separated into distinct channels.

We have incorporated the new Vectra Multispectral Imaging System (CRi) with its Inform software system into our analytical platform.

We have optimized FARSIGHT software for nuclear segmentation based on hematoxylin staining (see Publication #1).

We have developed FARSIGHT software for whole cell segmentation; the program segments cells in images stained for cytosolic and/or plasma membrane antigens and compartmentalizes each into nuclear and extranuclear compartments for the purpose of subcellular (nuclear vs. extranuclear) analyte quantification and distribution (see Publication #2).

### **Reportable Outcomes (Publication bibliography)**

#### ***Publication #1***

Al-Kofahi Y, Lassoued W, Lee WMF, and Roysam B: Improved automatic detection and segmentation of cell nuclei in histopathology images. *Trans. Biomed. Eng.* 57;841-852 (2010).

#### ***Publication #2***

Al-Kofahi Y, Lassoued W, Grama K, Nath SK, Zhu J, Oueslati R, Feldman M, Lee WMF, and Roysam B: Cell-based quantification of molecular biomarkers in histopathology specimens. (revision submitted to *Histopathology* – decision pending).

## **Abstracts**

2 Posters were presented at the ERA of Hope meeting in Baltimore, MD 2008

Personnel receiving pay: William Lee (PI, University of Pennsylvania, Philadelphia, PA)

Wiem Lassoued (research specialist, University of Pennsylvania, Philadelphia, PA)

Badrinath Roysam (co-PI, Rensselaer Polytechnic Institute, Troy, NY)

Youssef Al-Kofahi (graduate student, Rensselaer Polytechnic Institute, Troy, NY)

Kedar Grama (graduate student, Rensselaer Polytechnic Institute, Troy, NY)

## **Conclusions**

Multiple antigens reporting on prognostic/predictive biomarkers, cell signaling and cell fate decisions can be stained for on the same slide in human breast cancer specimens, along with markers of different subcellular compartments in tumor cells.

Following separation of staining for these analytes and subcellular compartment markers into separate channels by multispectral microscopy and spectral unmixing, image analysis can accurately and rapidly segment nuclei and cells in images and associate analytes with the segmented cells and subcellular compartments computationally.

## **References and Appendices**

### **Publication #1**

Al-Kofahi Y, Lassoued W, Lee WMF, and Roysam B: Improved automatic detection and segmentation of cell nuclei in histopathology images. Trans. Biomed. Eng 57;841-852 (2010).

### **Publication #2**

Al-Kofahi Y, Lassoued W, Grama K, Nath SK, Zhu J, Oueslati R, Feldman M, Lee WMF, and Roysam B: Cell-based quantification of molecular biomarkers in histopathology specimens. (revision submitted to *Histopathology*).

### **Pdf files of**

- (1) Publication #1
- (2) Publication #2
- (3) *Histopathology* decision letter
- (4) DD0882 Report of Inventions

are appended

# Improved Automatic Detection and Segmentation of Cell Nuclei in Histopathology Images

Yousef Al-Kofahi, Wiem Lassoued, William Lee, and Badrinath Roysam\*, *Senior Member, IEEE*

**Abstract**—Automatic segmentation of cell nuclei is an essential step in image cytometry and histometry. Despite substantial progress, there is a need to improve accuracy, speed, level of automation, and adaptability to new applications. This paper presents a robust and accurate novel method for segmenting cell nuclei using a combination of ideas. The image foreground is extracted automatically using a graph-cuts-based binarization. Next, nuclear seed points are detected by a novel method combining multiscale Laplacian-of-Gaussian filtering constrained by distance-map-based adaptive scale selection. These points are used to perform an initial segmentation that is refined using a second graph-cuts-based algorithm incorporating the method of alpha expansions and graph coloring to reduce computational complexity. Nuclear segmentation results were manually validated over 25 representative images (15 *in vitro* images and 10 *in vivo* images, containing more than 7400 nuclei) drawn from diverse cancer histopathology studies, and four types of segmentation errors were investigated. The overall accuracy of the proposed segmentation algorithm exceeded 86%. The accuracy was found to exceed 94% when only over- and undersegmentation errors were considered. The confounding image characteristics that led to most detection/segmentation errors were high cell density, high degree of clustering, poor image contrast and noisy background, damaged/irregular nuclei, and poor edge information. We present an efficient semiautomated approach to editing automated segmentation results that requires two mouse clicks per operation.

**Index Terms**—Image cytometry, cell nuclei, histopathology, segmentation.

## I. INTRODUCTION

THE GOAL of this study is to develop efficient and accurate algorithms for detecting and segmenting cell nuclei in 2-D histological images. This is commonly a first step to counting cells, quantifying molecular markers (antigens) of

interest in healthy and pathologic specimens [1], [2], and also for quantifying aspects of normal/diseased tissue architecture [1]. The cell nuclei may be stained using fluorescence markers [e.g., 4',6'-diamidino-2-phenylindole (DAPI)], or with histochemical stains (e.g., hematoxylin). It is important in these applications to be able to detect the correct number of cells with high accuracy, and to delineate them accurately with utmost automation and minimal human effort. It is also helpful to be able to easily adapt the software algorithms to images of different tissues captured under differing imaging conditions.

Automated segmentation of cell nuclei is now a well-studied topic for which a large number of algorithms have been described in the literature [2]–[18], and newer methods continue to be investigated. The main challenges in segmenting nuclei in histological, especially pathological tissue specimens, result from the fact that the specimen is a 2-D section of a 3-D tissue sample. The 2-D sectioning can result in partially imaged nuclei, sectioning of nuclei at odd angles, and damage due to the sectioning process. Furthermore, sections have finite thickness resulting in overlapping or partially superposed cells and nuclei in planar images. The end result of these limitations is a set of image objects that differ considerably from the ideal of round blob-like shapes. Their sizes and shapes in images can be irregular, and not always indicative of their 3-D reality. There is natural variability among nuclear shapes and sizes even when they are ideally sectioned. With pathological samples, nuclei can exhibit unnatural shapes and sizes. Variable chromatin texture is another source of segmentation error—highly textured nuclei are harder to segment, especially when they are densely clustered. Separation of densely clustered cell nuclei is a long-standing problem in this field. The presence of a large number of nuclei in the field (especially whole-slide images) necessitates methods that are computationally tractable, in addition to being effective. Finally, imaging noise in the background regions, especially for fluorescence data, and the presence of spectral unmixing errors in processed multispectral images results in additional errors.

Perhaps the most critical aspect of nuclear segmentation algorithms is the process of detecting a set of points in the image, usually one per cell nucleus and close to its center, that are variously referred to as “markers” or “seeds.” These points are used by subsequent algorithms to delineate the spatial extent of each cell nucleus. Indeed, the accuracy of the segmentation depends critically on the accuracy and reliability of the initial seed points. Several approaches have been used to detect seed points. The early work in this field [3], [19] relied upon the peaks of the Euclidean distance map. This method is often used in conjunction with the watershed algorithm [9] due to its computational efficiency and ready availability. However, it has

Manuscript received February 18, 2009; revised June 26, 2009. First published October 30, 2009; current version published March 24, 2010. This work was supported by the U.S. Army Breast Cancer Research Program under Grant W81XWH-07-1-0325 BC061142, by the National Institute of Biomedical Imaging and Bioengineering under Grant R01 EB005157, and by the National Science Foundation (NSF) under Grant EEC-9986821 to the Center for Subsurface Sensing and Imaging Systems. *Asterisk indicates corresponding author.*

Y. Al-Kofahi is with the Department of Electrical, Computer and Systems Engineering (ECSE), Rensselaer Polytechnic Institute, Troy, NY 12180 USA (e-mail: alkofy@rpi.edu).

W. Lassoued is with Dr. William's Lee Laboratory, Abramson Cancer Center, University of Pennsylvania, Philadelphia, PA 19104 USA (e-mail: wiem1las@yahoo.fr).

W. Lee is with the Division of Hematology-Oncology, Abramson Cancer Center, University of Pennsylvania, Philadelphia, PA 19104 USA (e-mail: leemingf@mail.med.upenn.edu).

\*B. Roysam is with the Department of Electrical, Computer and Systems Engineering (ECSE), Rensselaer Polytechnic Institute, Troy, NY 12180 USA (e-mail: roysam@ecse.rpi.edu).

Color versions of one or more of the figures in this paper are available online at <http://ieeexplore.ieee.org>.

Digital Object Identifier 10.1109/TBME.2009.2035102

the widely acknowledged disadvantage of detecting too many seeds, leading to over-segmentation. Some efforts at addressing this limitation include filtering of seeds based on mutual proximity [3], incorporation of additional cues such as the image intensity gradient [9], and the use of region merging algorithms as a postprocessing step [10], [11]. Another technique is to detect local maxima points in the gray-scale image using the  $h$ -maxima transform [16], [20]. This method was found to be overly sensitive to image texture, and resulted in overseeding with our images. The Hough transform [21] has also been used for detecting seed points [2], [6]. This method is practical for nearly circular nuclei, and requires excessive computation. More recently, the very elegant iterative radial voting algorithm was presented in [22], and has been used in several papers [14], [23]. This method requires edge extraction based on gradient thresholding, and a careful choice of several parameters that proved impractical in the automated pathology context. In [24] a regularized centroid transform was used. This method only uses the binarized image and does not exploit additional cues present in the image intensity data. In [8], a gradient flow-tracking algorithm was used. Like the radial voting idea, this method is conceptually elegant. The difficulty with this method in our experiments was the rough chromatin texture that produces inaccurate flow values and/or directions.

In this paper, we present a method that overcomes many of the limitations of the aforementioned methods. It is based on the multiscale Laplacian-of-Gaussian (LoG) filter originally introduced by Lindeberg [25] as a generic blob detection method. Recently, Byun *et al.* [4] used a blob detector based on the LoG filter at a fixed scale (set empirically) to count cells in retinal images. This method offers important advantages, including computational efficiency, ability to exploit shape and intensity information, ease of implementation, especially the ability to specify the approximate expected sizes of nuclei, and robustness to variations. Building upon this study, and keeping in mind the challenges specific to histopathology images noted earlier, we propose a method combining the LoG filter with automatic and adaptive scale selection.

Aside from advances in seed detection, the field of automated image analysis has also witnessed the emergence of a new generation of image segmentation algorithms. Notable among these advances are methods based on graph cuts [26]–[30] that offer the important advantage of computing globally optimal solutions. Additional advances have been reported across the literature. Notwithstanding these advances, several needs have remained. For instance, the graph-cuts algorithm requires effective initialization. For this, we present a method in which the results of seed detection are processed by a new generation of fast clustering algorithms to generate an initial segmentation that is subsequently refined using the graph-cuts segmentation algorithm. Another important need is to be able to segment large connected clusters of nuclei efficiently and accurately. For this, we introduce a novel segmentation algorithm based on automatic graph coloring and the method of  $\alpha$ -expansions. Overall, the effectiveness of the combination of these methods is demonstrated on breast histopathology images. Fig. 1 shows a flowchart illustrating the main steps of our method.

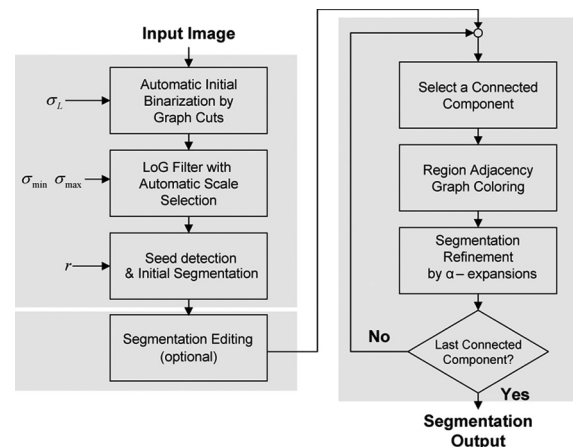


Fig. 1. Flowchart outlining the main steps of the proposed nuclear segmentation algorithm. The initial segmentation and refinement steps are illustrated in Fig. 2. The optional editing step is illustrated in Fig. 3.

## II. MATERIALS AND METHODS

### A. Histology and Nuclear Staining

For the *in vivo* tissue examples, deparaffinize  $5\ \mu\text{M}$  sections of formalin-fixed, paraffin-embedded human breast tissues were rehydrated, and stained with hematoxylin (Vector Laboratories, Burlingame, CA). For the *in vitro* tissue examples,  $6\ \mu\text{M}$  sections of OCT frozen blocks of cultured K1735 tumor cells were stained with DAPI (Vector Laboratories, Burlingame, CA).

### B. Image Capture

Images of hematoxylin or DAPI stained histopathology slides were captured using a Nuance multispectral camera (CRI, Inc., Woburn, MA) mounted on a Leica epifluorescence microscope (Leica DMRA2). Images were captured using full resolution of the Nuance camera at 8 bits of data per pixel and with 10 nm spectral widths from 420 to 720 nm for brightfield images, and 440–480 nm for DAPI. Nuance software was used to unmix the chromogens and fluorophore in the data cube into a set of nonoverlapping channels based on user-provided reference spectra of the pure chromogens or fluorochromes respectively. We denote the raw spectral data cube collected by the instrument  $I(x, y, \lambda)$ , where  $(x, y)$  are spatial coordinates of a pixel, and  $\lambda$  is the wavelength. The spectral unmixing procedure results in multiple nonoverlapping channels that are denoted as follows. The nuclear channel is denoted  $I_N(x, y)$ . This paper is primarily concerned with the processing of  $I_N(x, y)$ .

### C. Automatic Image Binarization

The first step in nuclear segmentation is to separate the foreground pixels in the nuclear channel  $I_N(x, y)$  from the background pixels. Several approaches have been presented in the literature, and a survey on image thresholding methods can be found in [31]. Common methods include histogram-based [32], clustering-based [33]–[35], and entropy-based [7] algorithms. More advanced techniques are based on graph-cuts [15] and level set [36] algorithms, but they require good



initialization/training. With this in mind, we propose a hybrid approach that starts with an initial binarization that is subsequently refined using the graph-cuts algorithm.

For the initial binarization, we compute the normalized image histogram, denoted  $h(i)$ , where  $i$  denotes the intensity of a pixel in the range  $\{0, \dots, I_{\max}\}$ . We found that 128 bins were adequate for these histograms. For the specimens studied here, the histograms were found to be bimodal as expected, and are modeled well by a mixture of two Poisson distributions. This modeling choice was supported by analysis of the image formation process [37], prior literature [37], and empirical comparison against the more commonly used mixture of Gaussians model [34], [38], [39]. We used the Poisson-distribution-based minimum error thresholding algorithm [38], [39]. The normalized image histogram for the mixture of Poisson distributions is written as

$$h(i) = P_0 \times p(i|0) + P_1 \times p(i|1) \quad (1)$$

where  $P_0$  and  $P_1$  are the *a priori* probabilities of the background and foreground regions, and  $p(i|j)$ ,  $j = 0, 1$  are Poisson distributions with means  $\mu_j$ . For a threshold  $t$ , the Poisson mixture parameters are given by

$$\begin{aligned} P_0(t) &= \sum_{i=0}^t h(i), & \mu_0(t) &= \frac{1}{P_0(t)} \sum_{i=0}^t i \times h(i) \\ P_1(t) &= \sum_{i=t+1}^{I_{\max}} h(i), & \mu_1(t) &= \frac{1}{P_1(t)} \sum_{i=t+1}^{I_{\max}} i \times h(i). \end{aligned} \quad (2)$$

The optimal threshold  $t^*$  is chosen to minimize an error criterion [38], as follows:

$$\begin{aligned} t^* &= \arg \min_t \{ \mu - P_0(t)(\ln P_0(t) + \mu_0(t) \ln \mu_0(t)) \\ &\quad - P_1(t)(\ln P_1(t) + \mu_1(t) \ln \mu_1(t)) \} \end{aligned} \quad (3)$$

where  $\mu$  is the mean intensity of the complete image. The result of thresholding  $I_N(x, y)$  using  $t^*$  is refined by incorporating spatial continuity constraints. We seek the pixel labeling  $L(x, y)$  that minimizes the following energy function:

$$\begin{aligned} E(L(x, y)) &= \sum_{(x, y)} D(L(x, y); I_N(x, y)) \\ &\quad + \sum_{(x, y)} \sum_{(x', y') \in N(x, y)} V(L(x, y), L(x', y')) \end{aligned} \quad (4)$$

where  $N(x, y)$  is a spatial neighbor of pixel  $(x, y)$ . The globally optimal labeling is computed using the widely used graph-cuts algorithm [26]–[30], [40], [41]. The first term in (4) is the data term representing the cost of assigning a label to a pixel. It has two possible values depending upon whether the foreground or background model is used. Mathematically, this is written as follows:

$$D(L(x, y); I_N(x, y)) = -\ln p(I_N(x, y)|j = \{0, 1\}). \quad (5)$$

The second term is the pixel continuity term that penalizes different labels for neighboring pixels. Following [26], this is

written as follows:

$$\begin{aligned} V(L(x, y), L(x', y')) &= \eta(L(x, y), L(x', y')) \\ &\quad \times \exp \left( -\frac{[I_N(x, y) - I_N(x', y')]}{2\sigma_L^2} \right) \end{aligned} \quad (6)$$

where

$$\eta(L(x, y), L(x', y')) = \begin{cases} 1, & \text{if } L(x, y) \neq L(x', y') \\ 0, & \text{if } L(x, y) = L(x', y'). \end{cases}$$

The  $V$ -term penalizes different labels for neighboring pixels when  $|I_N(x, y) - I_N(x', y')| < \sigma_L$ . In our work, the scale factor  $\sigma_L$  is set empirically to values in the range 20–30 pixels. Lower values are used when the image is smooth, and higher values are used when the nuclear chromatin is highly textured. We used an implementation of the fast max-fl w/min-cut algorithm described by Boykov and Kolmogorov [27]. The previous method results in accurate binarization results. Fig. 2(B) provides a visual example of the binarization results for the image in Fig. 2(A).

#### D. Automatic Seed Detection and Initial Segmentation

The graph-cuts binarization algorithm extracts connected clusters of nuclei that must be separated into individual nuclei. This requires identification of initial markers (a.k.a. seed points) such that there is one marker per cell. For the present work, multiscale LoG filter based approaches proved to be the most effective. The LoG filter is given by

$$\text{LoG}(x, y; \sigma) = \frac{\partial^2 G(x, y; \sigma)}{\partial x^2} + \frac{\partial^2 G(x, y; \sigma)}{\partial y^2} \quad (7)$$

where  $\sigma$  is the scale value, and  $G(x, y; \sigma)$  is a Gaussian with 0 mean and scale  $\sigma$ . When applied to an image containing blob-like objects, this filter produces a scale-selective peak response at the center of each object with radius  $r$  when  $r = \sigma\sqrt{2}$ . The main advantage of this filter is that the locations of these peaks are robust to the chromatin texture that has a much smaller scale value compared to the nuclear blobs. The filtering results form a topographic surface that provides a basis for cell segmentation. In addition, as we describe shortly, it provides additional useful information about the boundaries of touching nuclei. A direct application of the multiscale LoG to images of nuclei would be naïve, since our tissue specimens contain a heterogeneous population of cell types with different nuclear sizes. For this, we propose a multiscale LoG with automatic scale selection, as described by Lindeberg [25]. While this multiscale method greatly improved upon the fixed-scale method, as expected, it was nevertheless inadequate, as illustrated in Fig. 2(C) and (D). In particular, this method fails over heterogeneous clusters of nuclei with different sizes, and weak separating edges. In these cases, it is possible for clusters of 2 or more small nuclei to be detected falsely as a single larger blob that may also encroach on smaller blobs in its vicinity. Overcoming this issue requires a more sophisticated control over the scale values. Our

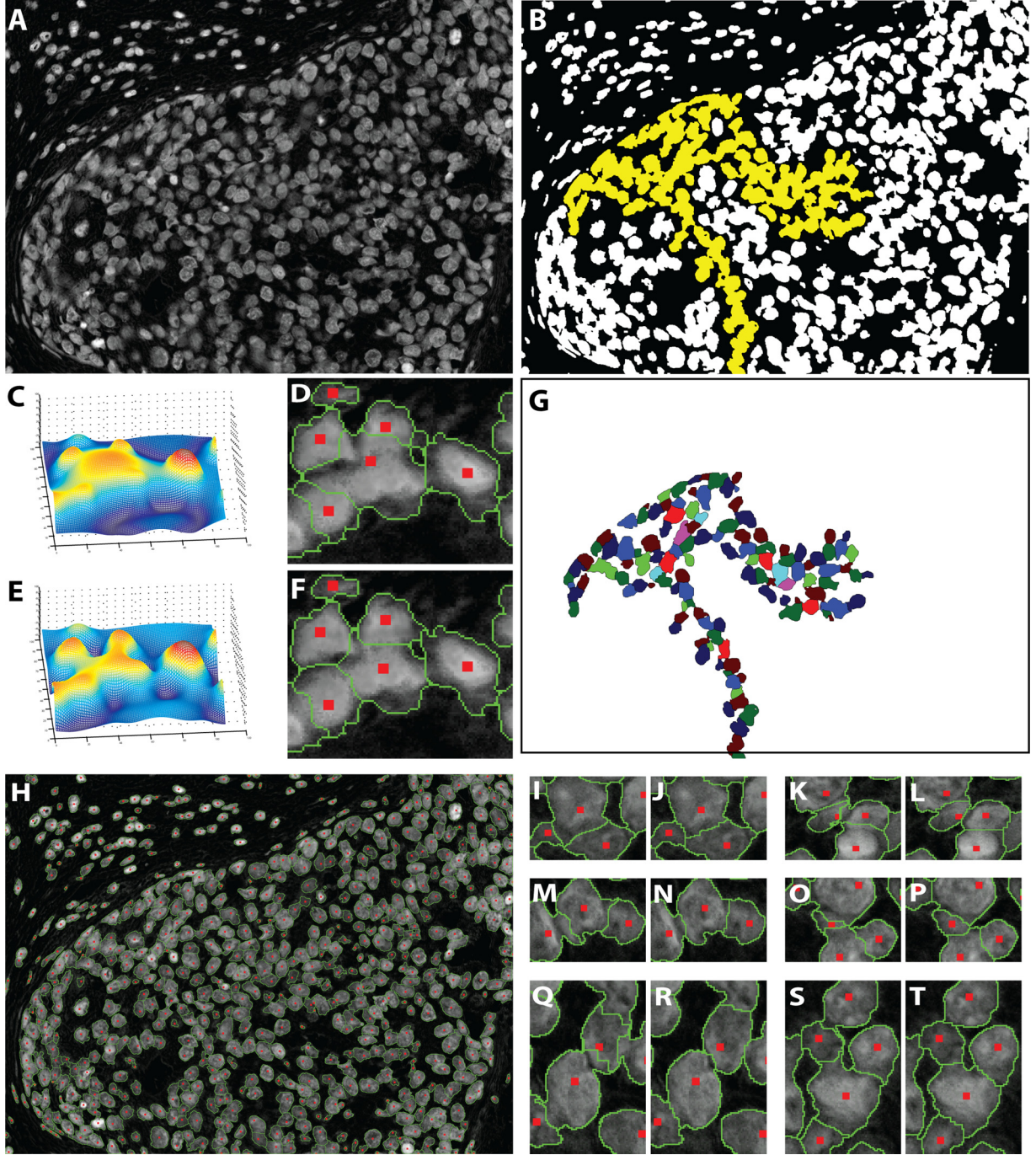


Fig. 2. Illustrating key steps of the proposed nuclear segmentation method. (A) Nuclear channel from spectral unmixing. (B) Foreground extraction results. Pixels marked yellow represent a large connected component. (C) Surface plot of the multiscale LoG filtering results for a small region. (D) Initial segmentation based on the LoG. (E) Surface plot of the distance-map-constrained multiscale LoG. (F) Improved initial segmentation resulting from the distance-constrained LoG. (G) Color coding of the yellow pixels in panel (B). (H) Final segmentation of the image in panel (A). Panels (I and J), (K and L), (M and N), (O and P), (Q and R), and (S and T) indicate initial and final segmentation closeups taken from different regions in the image shown in panel (H).

method to achieve such control relies on exploiting shape and size cues available in the Euclidean distance map  $D_N(x, y)$  of the binarized image [42], [43]. Our method proceeds as follows. We compute the response of the scale-normalized LoG filter  $\text{LoG}_{\text{norm}}(x, y; \sigma) = \sigma^2 \text{LoG}(x, y; \sigma)$  at multiple scales  $\sigma = [\sigma_{\min}, \dots, \sigma_{\max}]$  in steps of 1. Then, we use the Euclidean distance map to constrain the maximum scale values when com-

binning the LoG filtering results across scales to compute a single response surface denoted  $R_N(x, y)$  as follows:

$$R_N(x, y) = \arg \max_{\sigma \in [\sigma_{\min}, \sigma_{\max}]} \{ \text{LoG}_{\text{norm}}(x, y; \sigma) * I_N(x, y) \} \quad (8)$$

where  $\sigma_{\max} = \max\{\sigma_{\min}, \min\{\sigma_{\max}, 2 \times D_N(x, y)\}\}$ .



In effect, the distance map constrains the maximum scale value *at each point*. The response  $R_N(x, y)$  can be thought of as a topographical surface whose peaks indicate centers of individual nuclei—these are the seed points (nuclear markers). We identify the local maxima of  $R_N(x, y)$ , and impose a minimum size (based on the expected range of nuclear diameters) to filter out irrelevant minima, as described further in the following subsection. The effect of using the distance map constraint is illustrated in Fig. 2. For instance, panels (C) and (D) show a surface plot of the multiscale LoG and the corresponding initial segmentation (discussed shortly), respectively. Clearly, the central nucleus is oversmoothed and encroaches into its neighbors. The reason for the encroachment is the use of large  $\sigma_{\max}$  that is needed to detect large cells in other regions in the image. Fig. 2(E) and (F), respectively, shows surface plots of  $R_N(x, y)$  and the corresponding initial segmentation. It is clear that the accuracy of seed locations and the initial cells boundaries are much improved by imposing the scale constraint.

Using  $R_N(x, y)$  and the seed points detected, as described earlier, we compute an initial segmentation of the nuclei, as described shortly. The classical approach used by several authors (including ourselves) is based on the watershed algorithm, and its many variants and improvements [2], [3], [5], [9]–[11], [16], [44], [45]. This method has the advantage of speed, simplicity, absence of adjustable parameters and a degree of flexibility that results from being able to modify the underlying distance map. The main disadvantage of this algorithm for the present task is its sensitivity to even minor peaks in the distance map that results in over segmentation, and detection of tiny regions as objects. To address this problem, we propose an alternate method based on size-constrained clustering. The use of clustering for nuclear/cell segmentation is not new, and predates the watershed method, e.g., [44] and [46]. However, clustering methods have been computationally expensive and difficult to scale to large images. Recently, Wu *et al.* [47] described the local-maximum clustering algorithm [47] that overcomes the previous limitations, and paved the way for the present work. This algorithm has a resolution parameter  $r$  that is used to define a search area, denoted  $A(x, y)$  of size  $2r \times 2r$  around each pixel in  $R_N(x, y)$ . In a nutshell, this algorithm uses the seed points as cluster centers, and assigns each pixel in the foreground image to these centers to form clusters.

To illustrate the effect of varying the resolution parameter on the clustering (initial segmentation results), Fig. 3 shows two 1-D examples. The shown curve consists of several 1-D blobs with different sizes. When using a small resolution parameter ( $r = 3$ ) all the three blobs are detected. The local maxima (seed points) are indicated in dark red, and the vertical dashed-red lines separate the blobs. The direction and length of the black arrows indicate the assignment of each point to its local maximum in a region (distance in 1-D) defined by the resolution parameter. In panel (B), we use a larger value of the resolution parameter ( $r = 6$ ). Therefore, the small blob (center) is bypassed and pixels to its left are assigned to their local maxima points to its right. Only two blobs (with two corresponding seed points) were detected. Note that the separating lines pass through the minima between the two blobs. These points can be thought of as inflection

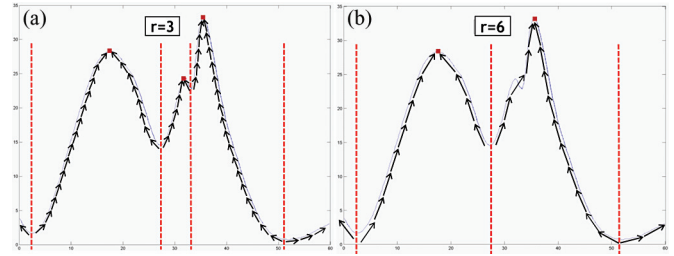


Fig. 3. Illustrating the local-maximum clustering method. A 1-D curve with three blobs is used. The blob in the middle is very small compared to the others. Two values for the resolution parameter are used. Using in panel (A) results in detecting all three blobs. In panel (B), the use of resulted in missing the small blob and merging it to the larger one on the right. The black arrows indicate the assignments of points to their local maxima. The detected seed points are displayed as red dots.

points, where one inflection point is present between blobs. In 2-D images, we have separating boundaries between 2-D blobs.

There are two major advantages of using this method over the watershed method [48]. First, the resolution parameter  $r$  provides the ability to avoid forming small clusters, as was clearly shown in the two synthetic examples of Fig. 3. Second, the clustering method works on foreground points only, which makes it faster. In our experiments, this algorithm was comparably fast to the watershed, and often faster. In our study, the parameter  $r$  was set empirically in the range of five pixels. Intuitively,  $r$  specifies the smallest size of the clusters that we are willing to accept for the next stage of processing.

#### E. Refinement of Initial Nuclear Segmentation using $\alpha$ -Expansions and Graph Coloring

The segmentation contours produced by the aforementioned cluster analysis are approximate because the clusters are formed using  $R_N(x, y)$  rather than the original image, and therefore require further refinement using the image intensity.

The purpose of the refinement is to enhance the initial contours between touching nuclei to better delineate the true edges between them. To meet this goal, three requirements are needed in the segmentation refinement step. First, it should preserve the shape of the cell nucleus based on some shape model. Second, there should be some rules that prevent two or more nuclei from being merged. This happens if we allow two nonneighbor nuclei to encroach into a third one between them until they merge. Third, given the large number of cell nuclei found in real images, the refinement step should allow multiple cell nuclei need to be refined concurrently for efficiency.

As with the binarization refinement this step is also formulated as an energy minimization that is solved using a graph-cuts algorithm. However, the problem here is more challenging since we have multiple labels, where the number of labels equals the number of cells in a connected component. In the binary case, the graph-cuts method finds the global minima in polynomial time. However, finding a multiway cut, such that the resulting labeling configuration minimizes the energy function is known to be NP-hard. Boykov *et al.* [29] introduced two algorithms, known as  $\alpha$ -expansion and  $\alpha - \beta$  swap, respectively, that can

efficiently find good approximate solutions to the multiway cut to within a known factor of the global minimum. In this study, the former is used. In the  $\alpha$ -expansion method, we formulate the segmentation as an iterative binary labeling problem. At each iteration, one label is set to an integer  $\alpha$ , and the rest of the labels are set to another value, denoted  $\bar{\alpha}$ , where  $\bar{\alpha} \neq \alpha$ . Then, a binary graph-cuts step (called an expansion) is carried out, in which pixel labels are allowed to change in one direction from  $\bar{\alpha}$  to  $\alpha$ . The border of the cell labeled with  $\alpha$  is refined by expanding it into its neighbors until the energy function is minimized. In the ideal case, the energy function will reach its minimum when the segmentation contour delineates the true nucleus contour, at which the gradient is maximum. The data and smoothness terms of the energy function should be chosen carefully in order to achieve that goal. For the  $\alpha$ -expansion method to work, the smoothness term denoted  $V$  has to be a metric that requires three conditions to hold [29]. Given any three pixel labels  $L_1$ ,  $L_2$ , and  $L_3$ , the three conditions are listed as follows:

- 1)  $V(L_1, L_2) = 0 \Leftrightarrow L_1 = L_2$ ;
- 2)  $V(L_1, L_2) = V(L_2, L_1) \geq 0$ ;
- 3)  $V(L_1, L_2) \leq V(L_1, L_3) + V(L_3, L_2)$ .

We used a spatially varying smoothness function similar to the one used in the binarization step

$$V(L(x, y), L(x', y')) = \eta(L(x, y), L(x', y')) \times \exp(-|I_N(x, y) - I_N(x', y')|)$$

where

$$\eta(L(x, y), L(x', y')) = \begin{cases} \text{Const}, & \text{if } L(x, y) \neq L(x', y') \\ 0, & \text{if } L(x, y) = L(x', y'). \end{cases}$$

The previous smoothness function is reached when the labeling discontinuities occur at the edges between the nuclei. The data term at each pixel depends on the likelihood of assigning it to each label (nucleus). As mentioned earlier, the LoG output profile of each nucleus is roughly similar to a Gaussian. In addition, the elliptical shape of the cell is similar to that of the 2-D Gaussian. Hence, a Gaussian model is used to represent each cell. A maximum likelihood method (MLE) is used to estimate the Gaussian parameters. The inputs to the MLE are the  $(x, y)$  coordinates of the pixels of each nucleus, weighted by the pixelwise LoG responses. The likelihood for a pixel  $(x, y)$  to be assigned to cell  $i$  is  $G(x, y; \mu_i, \Sigma_i)$ , where  $\mu_i$  and  $\Sigma_i$  are the mean and the covariance matrix of the  $i$ th Gaussian, respectively.

Unfortunately, the  $\alpha$ -expansion method is not practical when the number of cells in a connected component is large ( $>20$ ), leading to an excessive number of expansions that require an impractical amount of computer memory and time. To address this difficulty, we propose a novel method based on graph coloring that is described next. We start by noting that when the  $\alpha$ -expansion procedure is applied to an initially segmented cell, it will only expand to its neighboring regions. This is because the expansion procedure will not assign a pixel to a distant cell. Therefore, we turn the problem into using a small number of labels, with each having a large number of cells expanding in

parallel. This is achieved by using a graph coloring approach similar to the one used in [13], but we differ in the use of a two-level region adjacency graph. Using the initial segmentation, we build a region adjacency graph. Unlike our prior work [10], [11], we now use a two-level adjacency graph in which a cell is adjacent to its direct neighbors, and to the neighbors' neighbors as well. The second level of adjacency is added to reduce the possibility that two nonneighboring cells with the same color merge after an expansion. The graph is then colored sequentially such that no two adjacent cells have the same color. Choosing the number of colors is a challenge since the well-known four-color theorem [49] does not apply in our case because of our two-level structure. The problem of finding the minimal number of colors is nondeterministic polynomial-time hard (NP-hard). For these reasons, we use a sequential coloring method that is simple to implement, but does not necessarily yield the smallest number of colors. Fig. 2(G) shows the coloring output for the initial segmentation of a connected component. This connected component [also shown in yellow in the binarization, which is shown in Fig. 2(B)] contains 123 nuclei, but only eight colors are used.

The resulting colors are used as labels for the  $\alpha$ -expansion step. At each iteration, all the nuclei with a given color are assigned the label  $\alpha$ , while all others are assigned  $\bar{\alpha}$ . Then,  $\alpha$  cells are expanded concurrently into  $\bar{\alpha}$  cells. As a result, just a few (usually less than 10) expansions are needed regardless of the much larger number of cells in a connected cluster. The smoothness term described earlier is a pixel-level function, since it depends on the local gradient between adjacent pixels, and hence it is not affected by the grouping of cells based on graph coloring. On the other hand, the data term is a function defined on a cell level, since it is based on a Gaussian model of the cell. Therefore, it is modified in order to compute likelihoods to be assigned to groups (colors) rather than individual cells. Suppose that the number of colors assigned to a connected component with  $N_c$  cells is  $N_r$ , where  $N_r \ll N_c$ . The likelihood that a pixel  $(x, y)$  will be assigned the  $j$ th color is

$$p(L(x, y) = j) = \max \left\{ G\left(x, y; \mu_i, \sum_i\right) | C_i = j \right\}, \quad j = 1. \quad (9)$$

The corresponding data term that represents the penalty for assigning pixel  $(x, y)$  to color  $j$  is

$$D(L(x, y) = j; I_N(x, y)) = -\ln p(L(x, y) = j). \quad (10)$$

The segmentation refinement consists of multiple iterations of  $\alpha$ -expansion up to a preset maximum number of iterations (usually 3), or until no change in any pixel label will reduce the energy function. Finally, the resulting objects are renumbered to achieve consistency with the numbers of the initial objects. In Fig. 2, panels (I and J), (K and L), (M and N), (O and P), (Q and R), and (S and T), respectively, represent initial and refined segmentation closeups taken from different regions in the image shown in panel (H) of the same figure.

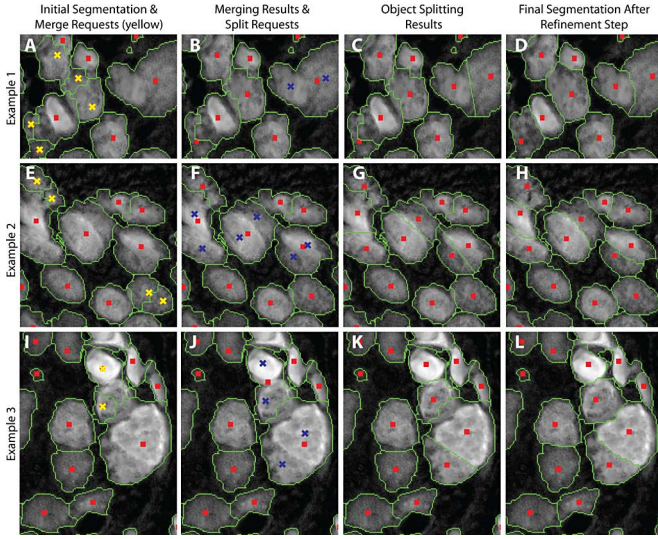


Fig. 4. Illustrating the impact of (optional) seed editing on the final segmentation. (A), (E), and (I) Initial segmentations are shown in the first column for three selected regions. Yellow crosses indicate locations of mouse clicks requesting pairs of segmented objects to be merged. (B), (F), and (J) Results of merging are shown in the second column, in addition to the user's requests to split objects indicated as blue crosses. The blue crosses are initial seeds locations for the two new objects. (C), (G), and (K) Results of splitting are shown in the third column. (D), (H), and (L) Final segmentation after refinement is shown in the fourth column.

#### F. Efficient Computer-Assisted Editing of Automated Segmentation Results

Automatic segmentation algorithms can provide fast and accurate segmentation of nuclei. However, segmentation errors cannot be avoided even when using optimal parameter values. Hence, human interaction might be needed to fix some of the segmentation errors in order to obtain the highest level of accuracy. Indeed, human interaction should be made minimal by tuning the segmentation parameters to reduce the number of errors. In addition, the editing method should be made easy and fast. In this study, two types of errors (defined in the next section) can be corrected using manual editing. The first type is over-segmentation and is corrected by merging fragments of oversegmented nuclei. The merging is performed on pairs of neighbor objects by clicking on one point inside each one of them. Fig. 4(A), (E), and (I) shows closeups of initial segmentation results. User selected points (using mouse clicks) for pair of objects that need to be merged are shown in yellow. The merging results are shown in Fig. 4(B), (F), and (J).

The second type of errors that can be corrected is under-segmentation. An undersegmented object is split into two objects by clicking at two points inside it. An automatic splitting method is used to draw an initial contour between the two new objects.

The splitting method starts by computing the approximate Euclidean distances from each point inside the undersegmented object to the manually selected points. Then, the splitting is done based on the minimum of the two distances at each point. Blue crosses in Fig. 4(B), (F), and (J) represent user selected pairs of points indicating objects that need to be split. Fig. 4(C), (G), and (K) shows the automatic splitting results. Changes to the initial

segmentation caused by editing are also applied on all the images needed in the segmentation refinement step. As illustrated previously, the refinement step uses a graph-cuts-based technique ( $\alpha$ -expansion), where both the initial segmentation and the LoG output  $[R_N(x, y)]$  are needed. The editing methods mentioned earlier will update the labels in the initial segmentation. On the other hand, the LoG output  $R_N(x, y)$  is updated as follows. In the case of oversegmentation, the LoG output profile of the oversegmented object is replaced by the inverted distance map from the center of the new object produced by merging. On the other hand, the LoG output profile of an oversegmented object is replaced by the inverted distance map from the centers of the two new objects resulting from splitting. Fig. 4(D), (H), and (L) shows the final segmentation after refinement. A related two-mouse-click based technique for interactive whole cell segmentation was presented in [50], where the user segments one cell at a time by clicking on a point at the center of cell and another one on its border. The image is then transformed into polar coordinates, a dynamic programming algorithm is used to find the optimal path on the cell border from left to right, and finally that path is mapped back into Cartesian coordinates.

One drawback of the presented editing tool is the need to scan the image visually to search for segmentation errors. This can be a time consuming task in very large images with large numbers of cells. One possible solution is to adopt the approach presented by the same group [51] in which a segmentation confidence score is computed for each segmented cell nucleus based on some morphological and intensity based features. The lower the confidence score, the more likely the segmentation error is. Then, segmented cell nuclei are sorted based on their confidence scores and the user starts inspecting those starting from those with low confidence values. Yet another approach that is explored as part of the FARSIGHT project ([www.farsight-toolkit.org](http://www.farsight-toolkit.org)) is to identify outliers (based on one or more features) to detect nuclei that require further inspection for potential editing. In general, the use of pattern analysis tools to guide the user for expedited editing is a topic of ongoing research.

### III. RESULTS AND VALIDATION

The results of automated analysis for 25 representative images (15 *in vitro* images and ten *in vivo* images, containing more than 7400 nuclei in all) drawn from diverse cancer histopathology studies were inspected and scored manually with the goal of developing a conservative assessment of the frequency and types of segmentation errors. The manual scoring was recorded electronically, and a sample is displayed in Fig. 5(A). In this figure the type of error is indicated as a color-coded dot. Seeds of correctly segmented nuclei are displayed as green dots. Undersegmentation errors (i.e., a failure to split a region into the correct number of nuclei) are indicated as dark blue dots. Oversegmentation errors (i.e., excessive splitting) are indicated as purple dots. In addition to these standard types of errors, we also looked for encroachment errors (indicated as yellow dots) that occur when the automated algorithms do not correctly place the boundary between a pair of touching nuclei. In other words, it is the error in delineating the true border between two



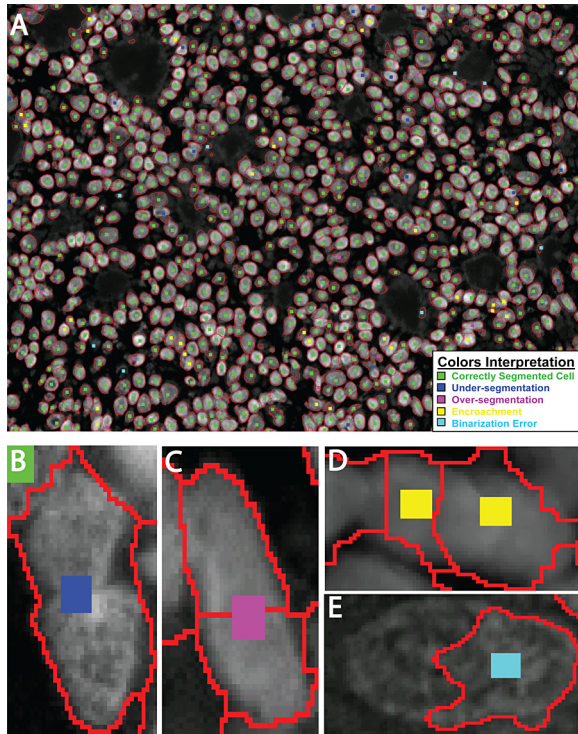


Fig. 5. Illustrating the results validation criteria. (A) Segmentation output of an image with color-coded seeds on each nucleus to identify whether it is correctly segmented or the type of segmentation error. (B) Example of an undersegmentation error. (C) Example of oversegmentation error. (D) Example of an encroachment error. (E) Example of a binarization error.

nuclei. The last type of segmentation errors is binarization errors. This type of error includes the case of nuclei encroaching on their neighbors, or nuclei encroached over by their neighbors. The main difficulty with quantification of encroachment errors is its innate subjectivity. Another difficulty is the acceptance threshold. In a strict sense, one could argue successfully that every adjacent pair of nuclei suffers from some encroachment error. In our work, a slight encroachment of a few pixels that does not change the nucleus shape or size significantly is not considered as an error. We only consider moderate to severe encroachment errors in which the error corresponds to at least 25% of the total nucleus area. Although this manual observation is still subjective and may vary from an observer to another, it can give a good approximation of the number of encroachment errors. Furthermore, we also examined errors from automatic binarization of the image data. The binarization is visualized as boundaries overlaid on the image [see Fig. 5(A)]. Incorrectly binarized nuclei are indicated with light blue dots in Fig. 5(A). We considered errors for which a cell nucleus or part of it is missed at the binarization step.

Finally, Fig. 6 shows six typical examples of segmented nuclear images. All of the scoring results are provided to the reader in the *electronic supplement* (available: [www.ecse.rpi.edu/~roysam/TBME-2010-Supp/](http://www.ecse.rpi.edu/~roysam/TBME-2010-Supp/)). Table I summarizes the error analysis using 25 images. The first 15 in the table are *in vitro* images while the last ten are *in vivo*. Overall, just considering under- and oversegmentation errors alone, our

fully automated algorithm achieved >94% accuracy. These data are helpful in comparing our algorithm to previously published methods [9], [18]. When encroachment and binarization errors are included, our algorithm showed an accuracy of more than 86%. The performance of our algorithm with regard to over- and undersegmentation errors can be described in terms of precision and recall measures. Specifically, the last two columns of these values are indicated in Table I. The overall *F*-measure ( $2 \times \text{precision} \times \text{recall} / (\text{precision} + \text{recall})$ ) for these data is 0.97. We studied the performance of our binarization refinement step by comparing its output with the initial binarization using twenty 2-D phantom images for which we have ground truth data. For each image, we compared the percentages of incorrectly labeled pixels before and after binarization refinement using graph cuts, as detailed in Table II. Fig. 7(A) and (B) shows a sample phantom image and the corresponding ground truth. Initial segmentation output is shown in panel (C), while the refinement output is shown in panel (D). It is clear that significant improvement is achieved after applying graph-cuts refinement.

Finally, we studied the complexity reduction achieved using graph coloring by comparing segmentation processing times with and without graph coloring for 15 automatically created phantom images. All the images have the same size ( $300 \times 300$ ), with only one connected component (cluster of nuclei), and a varying number of nuclei in each cluster (10–150). Table III shows a summary of the analysis. Increasing numbers of nuclei in the cluster results in rapidly increasing processing time when graph coloring is not used. That is because the number of required  $\alpha$ -expansions is equal to the number of nuclei in the cluster. However, no significant increase in processing time is noted when graph coloring is used, since the number of  $\alpha$ -expansions is equal to the number of colors, which is in the range of 5 to 10 colors. Three sample phantom images are shown in Fig. 8(A)–(C) containing 10, 70, and 130 nuclei, respectively. The segmentation results are shown as red outlines. A graphical representation of the results in Table III is shown in Fig. 8(D), which shows 2-D plots of the number of cells in the connected component (cluster) versus the processing time for both cases.

#### IV. DISCUSSION

The present work has built upon, integrated, and extended multiple recent advances in the biological image analysis field. The resulting algorithms have proved to be extremely robust and accurate. In our experience, the usually tricky task of choosing the optimal parameter settings for the proposed algorithm is both simple as well as intuitive. When errors do occur, our method of editing the seeds, followed by segmentation refinement is extremely efficient in practice. It requires minimal effort, and makes best use of the human observer's ability to discern complex patterns, and resolve ambiguities. The actual segmentation is best carried out computationally.

There are several known sources of the errors analyzed by us. Oversegmentation usually happens when a nucleus' chromatin is highly textured (especially true for large nuclei) or when the nucleus shape is extremely elongated. This is particularly common with nuclei that deviate significantly from a



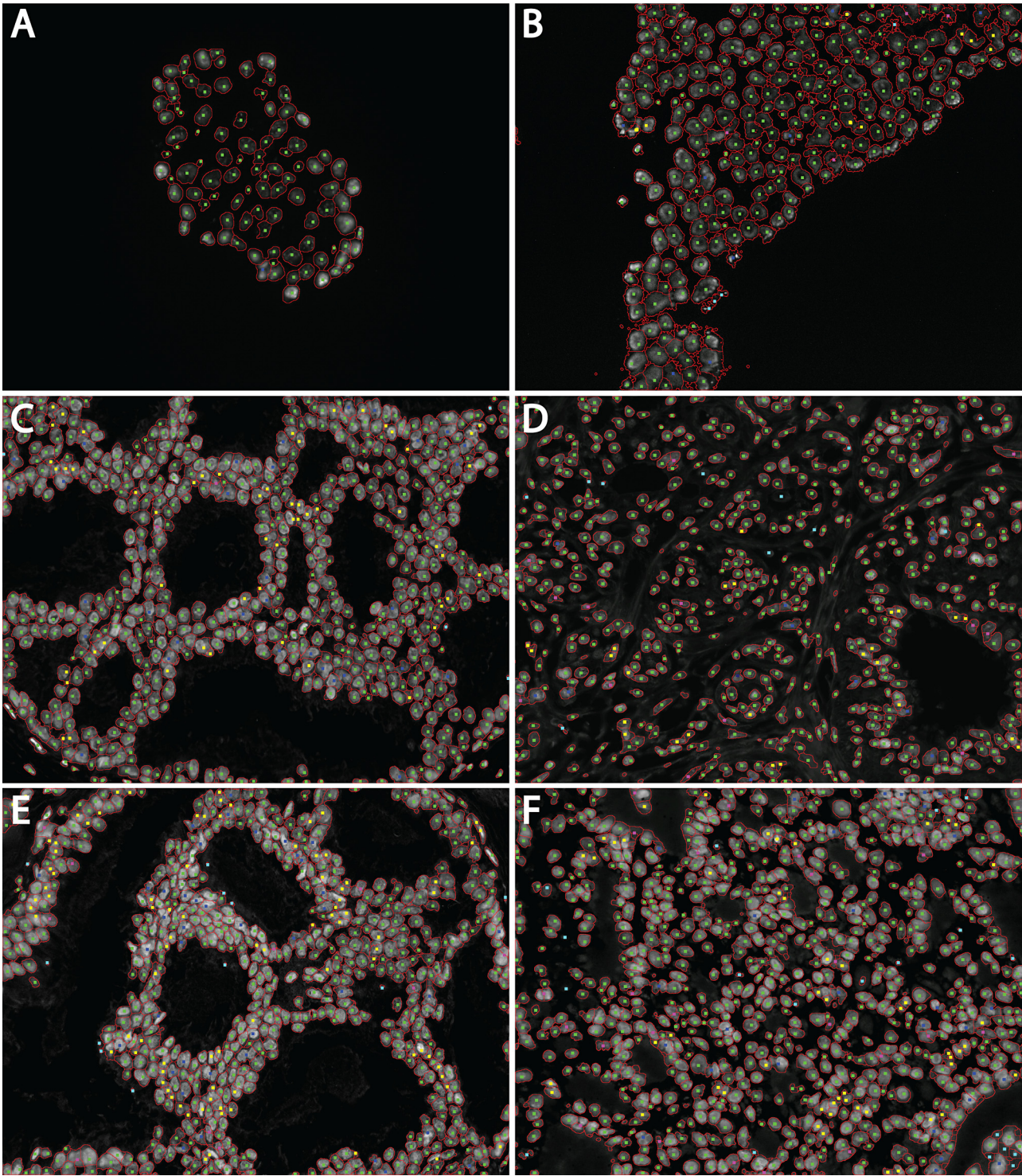


Fig. 6. Sample segmentation results of six 2-D nuclear images including [(A) and (B)] two *in vitro* images and [(C)–(F)] four *in vivo* images.

blob shape, as is the case with some vascular endothelial cells. Undersegmentation usually occurs when nuclei (especially small ones) are highly clustered with weak borders between the nuclei. The causes of encroachment errors were much more diverse, and most often caused by weak object separation cues in the image. The types of errors mentioned earlier are, to some extent, influenced by the choice of parameter settings. This is

discussed further shortly. Binarization errors were largely due to variations in the nuclear signal intensity, specifically, a weak signal resulted in most binarization errors.

A traditional difficulty with automated algorithms is the effort required to tune them by selecting appropriate parameter settings to new images and applications. In this regard, the algorithms we described are well-behaved and intuitive. The main

TABLE I  
SUMMARY OF SEGMENTATION PERFORMANCE DATA FOR 25 SAMPLE IMAGES\*

Image ID	Number of Cells	Correctly Segmented	Under-Segmented	Over-Segmented	Encroachment Errors	Binarization Errors	Precision	Recall
1	29	27	2	0	0	0	1.00	0.93
2	75	74	0	0	0	1	1.00	1.00
3	154	145	2	2	2	3	0.99	0.99
4	258	232	8	4	10	4	0.98	0.97
5	61	60	1	0	0	0	1.00	0.98
6	98	84	6	2	2	4	0.98	0.93
7	97	96	1	0	0	0	1.00	0.99
8	59	55	1	0	1	2	1.00	0.98
9	53	47	2	1	0	3	0.98	0.96
10	33	33	0	0	0	0	1.00	1.00
11	71	63	3	0	2	3	1.00	0.95
12	34	34	0	0	0	0	1.00	1.00
13	153	148	2	0	1	2	1.00	0.99
14	56	43	6	2	3	2	0.96	0.88
15	156	143	6	2	3	2	0.99	0.96
16	637	487	40	10	89	11	0.98	0.92
17	627	532	33	3	55	4	0.99	0.94
18	375	317	12	11	9	26	0.97	0.96
19	766	644	29	24	50	19	0.96	0.96
20	873	779	25	14	36	19	0.98	0.97
21	641	531	33	17	49	11	0.97	0.94
22	575	491	38	3	37	6	0.99	0.93
23	563	498	11	16	27	11	0.97	0.98
24	608	512	32	12	40	12	0.98	0.94
25	401	344	25	3	17	12	0.99	0.93
<b>Total</b>	<b>7441</b>	<b>6419</b>	<b>312</b>	<b>125</b>	<b>430</b>	<b>155</b>	<b>0.98</b>	<b>0.95</b>
<b>Percentage</b>		<b>86.3%</b>	<b>4.2%</b>	<b>1.7%</b>	<b>5.8%</b>	<b>2.1%</b>		

\*All of the images and segmentation results are available as an electronic supplement of facilitate high-resolution viewing.

TABLE II  
COMPARISON OF BINARIZATION ACCURACY BEFORE AND AFTER GRAPH-CUT REFINEMENT

Image ID	Error in initial binarization (%)	Error after refinement (%)
1	3.3	1.4
2	5.8	3.0
3	9.0	4.1
4	10.7	3.8
5	13.4	5.1
6	13.4	6.0
7	14.0	6.2
8	13.2	5.5
9	12.8	6.5
10	12.1	5.6
11	12.3	6.2
12	11.5	5.4
13	11.7	6.3
14	12.7	6.1
15	11.2	5.2
16	13.2	6.2
17	11.1	5.3
18	12.4	5.1
19	12.8	6.2
20	13.5	6.4
<b>Average</b>	<b>11.4</b>	<b>5.3</b>

parameters that must be provided to the software include the minimum scale for the LoG filter  $\sigma_{\min}$ , the maximum scale value  $\sigma_{\max}$ , which define the expected range of sizes of the nuclei. In our experiments, we used values in the range of four to eight pixels for  $\sigma_{\min}$ , and 10–20 pixels for  $\sigma_{\max}$ . Although our algorithms are multiscale by design, the choice of these

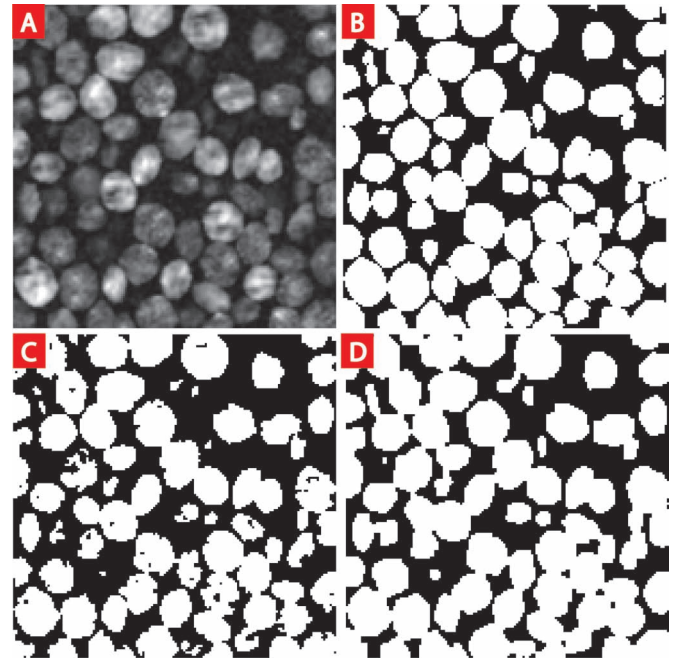


Fig. 7. Comparing initial and graph-cut refined binarization results using a phantom image for which the ground truth is known. (A) 2-D phantom image. (B) Binarization ground truth. (C) Initial binarization output. (D) Results of binarization refinement using graph cuts.

TABLE III  
ILLUSTRATING THE COMPLEXITY AND PROCESSING TIME REDUCTION AFTER USING GRAPH COLORING

Image ID	True number of cells	Number of Detected cells	Number of Colors Used	Segmentation Time (seconds)	
				Without coloring	With coloring
1	10	10	5	5.047	4.782
2	20	20	7	6.235	5.094
3	30	30	6	8.204	5.422
4	40	35	7	7.422	5.281
5	50	47	8	9.031	5.828
6	60	58	9	15.282	6.031
7	70	67	8	19.188	6.844
8	80	79	9	20.516	7.003
9	90	93	8	20.626	6.672
10	100	97	10	27.204	7.547
11	110	104	10	26.001	8.625
12	120	113	8	32.563	7.672
13	130	124	10	37.267	8.235
14	140	137	9	40.032	8.328
15	150	142	9	43.079	8.156

parameters affects the balance of over- and undersegmentation errors to a small extent. Between these two parameters,  $\sigma_{\min}$  is more influential. Specifically, if the value of  $\sigma_{\min}$  is much smaller than the expected minimum size of the nuclei, then the incidence of oversegmentation increases. Smaller values of this parameter are also needed to account for small fragments of nuclei that are characteristic of 2-D sections of 3-D tissue. On the other hand, if the value of  $\sigma_{\max}$  is too low, oversegmentation errors become more prevalent. An overly high value of  $\sigma_{\max}$  is much more benign in nature because it is used in combination with the distance map—it can result in undersegmentation or encroachment errors when exceptionally large and highly clustered groups of nuclei are encountered. The clustering resolution parameter  $r$  was generally chosen in the range of 3–5 pixels, and the weighting parameter  $\sigma_L$  for the graph-cuts segmentation algorithm was in the range of 20–30.



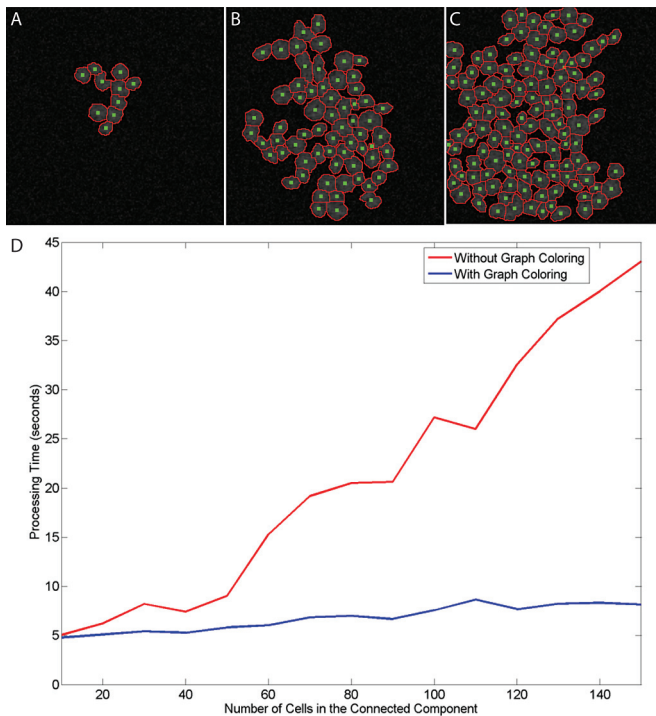


Fig. 8. Illustrating the effect of graph coloring using 15 phantom images with the same size and one nuclear cluster, but with different number of nuclei ( $x$ -axis). Three examples are shown in (A)–(C) containing 10, 70, and 130 nuclei, respectively. Detected seeds are shown as green dots and nuclear segmentation results are shown as red outlines. (D) Number of cell nuclei in the cluster versus segmentation processing time (without graph coloring in red and with graph coloring in blue).

The algorithm described here is incorporated into the FARSIGHT toolkit [51] that is designed to analyze multiparameter histopathology images. This software system and implementations of the algorithms reported here are available to interested colleagues from the corresponding author.

#### ACKNOWLEDGMENT

The authors wish to thank Dr. S. Nath for helpful discussions.

#### REFERENCES

- [1] C. Bilgin, C. Demir, C. Naci, and B. Yener, "Cell-graph mining for breast tissue modeling and classification," in *Proc. 29th Annu. Int. Conf. IEEE Eng. Med. Biol. Soc. (EMBS 2007)*, pp. 531–5314.
- [2] C. Ortiz de Solorzano, E. Garcia Rodriguez, A. Jones, D. Pinkel, J. W. Gray, D. Sudar, and S. J. Lockett, "Segmentation of confocal microscope images of cell nuclei in thick tissue sections," *J. Microsc.*, vol. 193, no. 3, pp. 212–226, Mar. 1999.
- [3] H. Ancin, B. Roysam, T. E. Dufresne, M. M. Chestnut, G. M. Ridder, D. H. Szarowski, and J. N. Turner, "Advances in automated 3-D image analyses of cell populations imaged by confocal microscopy," *Cytometry*, vol. 25, no. 3, pp. 221–234, Nov. 1, 1996.
- [4] J. Y. Byun, M. R. Verardo, B. Sumengen, G. P. Lewis, B. S. Manjunath, and S. K. Fisher, "Automated tool for the detection of cell nuclei in digital microscopic images: Application to retinal images," *Mol. Vis.*, vol. 12, no. 105–107, pp. 949–960, Aug. 16, 2006.
- [5] M. K. Chawla, G. Lin, K. Olson, A. Vazdarjanova, S. N. Burke, B. L. McNaughton, P. F. Worley, J. F. Guzowski, B. Roysam, and C. A. Barnes, "3D-catFISH: a system for automated quantitative three-dimensional compartmental analysis of temporal gene transcription activity imaged by fluorescence in situ hybridization," *J. Neurosci. Methods*, vol. 139, no. 1, pp. 13–24, Oct. 15, 2004.
- [6] C. O. De Solorzano, R. Malladi, S. A. Lelievre, and S. J. Lockett, "Segmentation of nuclei and cells using membrane related protein markers," *J. Microsc. Oxford*, vol. 201, pp. 404–415, Mar. 2001.
- [7] P. R. Gudla, K. Nandy, J. Collins, K. J. Meaburn, T. Misteli, and S. J. Lockett, "A high-throughput system for segmenting nuclei using multiscale techniques," *Cytometry A*, vol. 73, no. 5, pp. 451–466, May 2008.
- [8] G. Li, T. M. Liu, J. X. Nie, L. Guo, J. Malicki, A. Mara, S. A. Holley, W. M. Xia, and S. T. C. Wong, "Detection of blob objects in microscopic zebrafish images based on gradient vector diffusion," *Cytometry A*, vol. 71A, no. 10, pp. 835–845, Oct. 2007.
- [9] G. Lin, U. Adiga, K. Olson, J. F. Guzowski, C. A. Barnes, and B. Roysam, "A hybrid 3D watershed algorithm incorporating gradient cues and object models for automatic segmentation of nuclei in confocal image stacks," *Cytometry A*, vol. 56, no. 1, pp. 23–36, Nov. 2003.
- [10] G. Lin, M. K. Chawla, K. Olson, C. A. Barnes, J. F. Guzowski, C. Bjornsson, W. Shain, and B. Roysam, "A multi-model approach to simultaneous segmentation and classification of heterogeneous populations of cell nuclei in 3D confocal microscope images," *Cytometry A*, vol. 71, no. 9, pp. 724–736, Sep. 2007.
- [11] G. Lin, M. K. Chawla, K. Olson, J. F. Guzowski, C. A. Barnes, and B. Roysam, "Hierarchical, model-based merging of multiple fragments for improved three-dimensional segmentation of nuclei," *Cytometry A*, vol. 63, no. 1, pp. 20–33, 2005.
- [12] S. K. Nath, F. Bunyak, and K. Palaniappan, "Robust tracking of migrating cells using four-color level set segmentation," *Lect. Notes Comput. Sci. (ACIVS)*, vol. 4179, pp. 920–932, 2006.
- [13] S. K. Nath, K. Palaniappan, and F. Bunyak, "Cell segmentation using coupled level sets and graph-vertex coloring," in *Proc. Med. Image Comput. Comput.-Assisted Intervention (MICCAI)*, 2006, vol. 4190, pp. 101–108.
- [14] B. Parvin, Q. Yang, J. Han, H. Chang, B. Rydberg, and M. H. Barcellos-Hoff, "Iterative voting for inference of structural saliency and characterization of subcellular events," *IEEE Trans. Image Process.*, vol. 16, no. 3, pp. 615–623, Mar. 2007.
- [15] C. Russell, D. Metaxas, C. Restif, and P. Torr, "Using the P<sup>n</sup> Potts model with learning methods to segment live cell images," in *Proc. IEEE 11th Int. Conf. Comput. Vis.*, 2007, pp. 1–8.
- [16] C. Wahlby, I. M. Sintorn, F. Erlandsson, G. Borgefors, and E. Bengtsson, "Combining intensity, edge and shape information for 2D and 3D segmentation of cell nuclei in tissue sections," *J. Microsc. Oxford*, vol. 215, pp. 67–76, Jul. 2004.
- [17] M. Wang, X. Zhou, F. Li, J. Huckins, R. W. King, and S. T. Wong, "Novel cell segmentation and online SVM for cell cycle phase identification in automated microscopy," *Bioinformatics*, vol. 24, no. 1, pp. 94–101, Jan. 1, 2008.
- [18] G. Li, T. Liu, A. Tarokh, J. Nie, L. Guo, A. Mara, S. Holley, and S. T. Wong, "3D cell nuclei segmentation based on gradient flow tracking," *BMC Cell Biol.*, vol. 8, p. 40, 2007.
- [19] N. Malpica, C. O. de Solorzano, J. J. Vaquero, A. Santos, I. Vallcorba, J. M. Garcia-Sagredo, and F. del Pozo, "Applying watershed algorithms to the segmentation of clustered nuclei," *Cytometry*, vol. 28, no. 4, pp. 289–297, Aug. 1, 1997.
- [20] P. Soille, *Morphological Image Analysis: Principles and Applications*. Berlin, Germany: Springer-Verlag Telos, 1999.
- [21] D. H. Ballard, "Generalizing the hough transform to detect arbitrary shapes," *Pattern Recognit.*, vol. 13, no. 2, pp. 111–122, 1981.
- [22] Q. Yang and B. Parvin, "Perceptual organization of radial symmetries," in *Proc. IEEE Comput. Soc. Conf. Comput. Vis. Pattern Recognit.*, 2004, pp. 320–325.
- [23] H. Chang, Q. Yang, and B. Parvin, "Segmentation of heterogeneous blob objects through voting and level set formulation," *Pattern Recognit. Lett.*, vol. 28, no. 13, pp. 1781–1787, Oct. 1, 2007.
- [24] Q. Yang and B. Parvin, "Harmonic cut and regularized centroid transform for localization of subcellular structures," *IEEE Trans. Biomed. Eng.*, vol. 50, no. 4, pp. 469–475, Apr. 2003.
- [25] T. Lindeberg, "Feature detection with automatic scale selection," *Int. J. Comput. Vis.*, vol. 30, no. 2, pp. 79–116, Nov. 1998.
- [26] Y. Boykov and G. Funka-Lea, "Graph cuts and efficient N-D image segmentation," *Int. J. Comput. Vis.*, vol. 70, no. 2, pp. 109–131, Nov. 2006.
- [27] Y. Boykov and V. Kolmogorov, "An experimental comparison of min-cut/max-flow algorithms for energy minimization in vision," *IEEE Trans. Pattern Anal. Mach.*, vol. 26, no. 9, pp. 1124–1137, Sep. 2004.

- [28] Y. Boykov and M.-P. Jolly, "Interactive graph cuts for optimal boundary & region segmentation of objects in N-D images," in *Proc. Int. Conf. Comput. Vision*, 2001, pp. 1025–1112.
- [29] Y. Boykov, O. Veksler, and R. Zabih, "Fast approximate energy minimization via graph cuts," *IEEE Trans. Pattern Anal. Mach. Intell.*, vol. 23, no. 11, pp. 1222–1239, Nov. 2001.
- [30] V. Kolmogorov and R. Zabih, "What energy functions can be minimized via graph cuts?" *IEEE Trans. Pattern Anal. Mach. Intell.*, vol. 26, no. 2, pp. 147–159, Feb. 2004.
- [31] M. Sezgin and B. Sankur, "Survey over image thresholding techniques and quantitative performance evaluation," *J. Electron. Imag.*, vol. 13, no. 1, pp. 146–168, Jan. 2004.
- [32] R. Guo and S. M. Pandit, "Automatic threshold selection based on histogram modes and a discriminant criterion," *Mach. Vis. Appl.*, vol. 10, no. 5–6, pp. 331–338, Apr. 1998.
- [33] J. Kittler and J. Illingworth, "On threshold selection using clustering criteria," *IEEE Trans. Syst., Man, Cybern.*, vol. SMC-15, no. 5, pp. 652–655, Sep. 1985.
- [34] J. Kittler and J. Illingworth, "Minimum error thresholding," *Pattern Recognit.*, vol. 19, no. 1, pp. 41–47, 1986.
- [35] N. Otsu, "Threshold selection method from Gray-level histograms," *IEEE Trans. Syst., Man, Cybern.*, vol. SMC-9, no. 1, pp. 62–66, Jan. 1979.
- [36] J. Lie, M. Lysaker, and X. C. Tai, "A binary level set model and some applications to Mumford-Shah image segmentation," *IEEE Trans. Image Process.*, vol. 15, no. 5, pp. 1171–1181, May 2006.
- [37] N. R. Pal and S. K. Pal, "Image model, Poisson distribution and object extraction," *Int. J. Pattern Recognit. Artif. Intell.*, vol. 5, no. 3, pp. 459–483, 1991.
- [38] J. L. Fan, "Notes on Poisson distribution-based minimum error thresholding," *Pattern Recognit. Lett.*, vol. 19, no. 5–6, pp. 425–431, Apr. 1998.
- [39] N. R. Pal and D. Bhandari, "On object background classification," *Int. J. Syst. Sci.*, vol. 23, no. 11, pp. 1903–1920, Nov. 1992.
- [40] Y. Boykov, O. Veksler, and R. Zabih, "Markov random field with efficient approximations," in *Proc. IEEE Conf. Comput. Vis. Pattern Recognit.*, 1998, pp. 648–655.
- [41] D. Geiger, A. Gupta, L. A. Costa, and J. Vlontzos, "Dynamic programming for detecting, tracking, and matching deformable contours (vol 17, pg 294 1995)," *IEEE Trans. Pattern Anal. Mach. Intell.*, vol. 18, no. 5, pp. 575–575, May 1996.
- [42] J. Gill, H. Breu, D. Kirkpatrick, and M. Werman, "Linear time Euclidean distance transform algorithms," *IEEE Trans. Pattern Anal. Mach. Intell.*, vol. 17, no. 5, pp. 529–533, May 1995.
- [43] O. Cuisenaire, "Fast Euclidean distance transformations by propagation using multiple neighbourhoods," *Comput. Vis. Image Understanding*, vol. 76, no. 2, pp. 163–172, Nov. 1999.
- [44] R. W. Mackin, B. Roysam, T. J. Holmes, and J. N. Turner, "Automated three-dimensional image analysis of thick and overlapped clusters in cytologic preparations. Application to cytologic smears," *Anal. Quant. Cytol. Histol.*, vol. 15, no. 6, pp. 405–417, Dec. 1993.
- [45] R. W. Mackin, Jr., L. M. Newton, J. N. Turner, and B. Roysam, "Advances in high-speed, three-dimensional imaging and automated segmentation algorithms for thick and overlapped clusters in cytologic preparations. Application to cervical smears," *Anal. Quant. Cytol. Histol.*, vol. 20, no. 2, pp. 105–121, Apr. 1998.
- [46] B. Roysam, H. Ancin, A. K. Bhattacharjya, M. A. Chisti, R. Seegal, and J. N. Turner, "Algorithms for automated characterization of cell populations in thick specimens from 3-D confocal fluorescence microscopy data," *J. Microsc.*, vol. 173, no. 2, pp. 115–126, Feb. 1994.
- [47] X. W. Wu, Y. D. Chen, B. R. Brooks, and Y. A. Su, "The local maximum clustering method and its application in microarray gene expression data analysis," *EURASIP J. Appl. Signal Process.*, vol. 2004, no. 1, pp. 53–63, Jan. 1, 2004.
- [48] L. Vincent and P. Soille, "Watersheds in digital spaces—an efficient algorithm based on immersion simulations," *IEEE Trans. Pattern Anal. Mach. Intell.*, vol. 13, no. 6, pp. 583–598, Jun. 1991.
- [49] N. Robertson, D. P. Sanders, P. Seymour, and R. Thomas, "Efficient four-coloring planar graphs," in *Proc. 28th Annu. ACM Symp. Theory Comput.*, 1996, pp. 571–575.
- [50] D. Baggett, M. A. Nakaya, M. McAuliffe, T. P. Yamaguchi, and S. Lockett, "Whole cell segmentation in solid tissue sections," *Cytometry A*, vol. 67, no. 2, pp. 137–143, Oct. 2005.
- [51] C. S. Björnsson, G. Lin, Y. Al-Kofahi, A. Narayanaswamy, K. L. Smith, W. Shain, and B. Roysam, "Associative image analysis: a method for automated quantification of 3D multi-parameter images of brain tissue," *J. Neurosci. Methods*, vol. 170, no. 1, pp. 165–178, May 15, 2008.

**Yousef Al-Kofahi** received the B.S. degree in computer engineering from Yarmouk University, Irbid, Jordan, in 2003, and the M.S. degree in 2005 from the Electrical, Computer and Systems Engineering (ECSE) Department, Rensselaer Polytechnic Institute (RPI), Troy, NY, where he is currently working toward the Ph.D. degree in computer systems engineering.

He is currently engaged in developing computer vision and machine-learning algorithms for object-level mapping of complex biological tissues from 2-D/3-D multispectral images. His current research interests include computer vision, pattern recognition, and image processing/analysis.

**Wiem Lassoued** received the Master's degree in sciences from the University of Sciences of Tunis, Tunisia, in 2001.

She has been a Specialist Researcher C with Dr. William's Lee Laboratory, Abramson Cancer Center, University of Pennsylvania, Philadelphia, PA, for the past 5 years. Her current research interests include development of computerized quantitative analysis of histopathology tumor specimen based on image analysis, and look at different mechanisms involved to develop cancer.

**William Lee** received the Ph.D. and M.D. degrees from the University of Chicago, Chicago, IL, in 1974 and 1975, respectively.

He is currently an Associate Professor of medicine with the Division of Hematology–Oncology, University of Pennsylvania, Philadelphia, PA, where he also the Co-leader of the Tumor Biology Program in the Abramson Cancer Center. He is an Associate Editor of the *Journal of Clinical Investigation*. His current research interests include development of methods for quantitative analysis of human tumor histopathology and the biological events and processes preserved in these specimens.

**Badrinath Roysam** (SM'89) received the B.Tech. degree in electronics engineering from the Indian Institute of Technology Madras, Chennai, India, in 1984, and the M.S. and D.Sc. degrees from Washington University, St. Louis, in 1987, and 1989, respectively.

Since 1989, he has been with the Rensselaer Polytechnic Institute, Troy, New York, where he is currently a Professor in the Electrical, Computer and Systems Engineering Department. He is an Associate Director of the Center for Subsurface Sensing and Imaging Systems (CenSSIS)—a multiuniversity National Science Foundation (NSF) sponsored engineering research center, and the Co-director of the Rensselaer Center for Open Source Software. He also holds an appointment in the Biomedical Engineering Department. His current research interests include 2-D, 3-D, and 4-D biomedical image analysis, biotechnology automation, optical instrumentation, high-speed and real-time computing architectures, and parallel algorithms.

Dr. Roysam is a Senior Member the Microscopy Society of America, the International Society for Analytical Cytology, the Society for Neuroscience, and the Association for Research in Vision and Ophthalmology. He is an Associate Editor for the IEEE TRANSACTIONS ON BIOMEDICAL ENGINEERING and the IEEE TRANSACTIONS ON INFORMATION TECHNOLOGY IN BIOMEDICINE.

## **Cell-based Quantification of Molecular Biomarkers in Histopathology Specimens**

Yousef Al-Kofahi<sup>1,‡</sup>, Wiem Lassoued<sup>2,5‡</sup>, Kedar Grama<sup>3</sup>, Sumit K. Nath<sup>1</sup>, Jianliang Zhu<sup>2</sup>, Ridha Oueslati<sup>5</sup>,  
Michael Feldman<sup>4</sup>, William M. F. Lee<sup>2</sup>, Badrinath Roysam<sup>1,3</sup>

<sup>‡</sup>These two authors have contributed equally to this work.

<sup>1</sup>Department of Electrical, Computer and Systems Engineering, Rensselaer Polytechnic Institute, Troy, NY  
12180, USA.

<sup>2</sup>Department of Medicine, Abramson Cancer Center, University of Pennsylvania, Philadelphia, PA 19104,  
USA.

<sup>3</sup>Department of Biomedical Engineering, Rensselaer Polytechnic Institute, Troy, NY 12180, USA.

<sup>4</sup>Department of Pathology and Laboratory Medicine, Abramson Cancer Center, University of Pennsylvania,  
Philadelphia, PA 19104.

<sup>5</sup>Unit of IMEC, University of Sciences Bizerte, Tunisia.

**Correspondence:** Badrinath Roysam, JEC 7010, Rensselaer Polytechnic Institute, 110 8<sup>th</sup> Street, Troy, NY 12180. Phone: 518 276 8067, Email: [roysam@ecse.rpi.edu](mailto:roysam@ecse.rpi.edu), and William M. F. Lee, Abramson Cancer Center, University of Pennsylvania, Philadelphia, PA 19104. Phone: (215) 898 0258, Email: [leemingf@mail.upenn.edu](mailto:leemingf@mail.upenn.edu).

**Running Title:** Cell based biomarker quantification

**Key words:**

Digital histopathology,  
Molecular biomarkers,  
Cell typing,  
Multi-spectral Imaging  
Multiplexed Immunolabeling  
Automated Image Analysis

**Acknowledgments:** Various portions of this work were supported by S-IDEA grant W81XWH-07-1-0325 from the U.S. Army Breast Cancer Research Program, NIH grant R01 EB005157, NIH grant RO1 CA135509, and by NSF grant EEC-9986821. Portions of this project were funded by a grant from the Pennsylvania Department of Health. The Department specifically disclaims responsibility for any analysis, interpretations or conclusions. The authors thank Dr. Cliff Hoyt (CRi, Woburn, MA) for helpful discussions, and the staff at CRi Inc. for technical assistance.

## ABSTRACT

**Aims:** A computer-assisted technology for objective, cell-based quantification of molecular biomarkers in specified cell types in histopathology specimens to advance current visual estimation or pixel-level (rather than cell based) quantification methods.

**Methods:** Tissue specimens are multiplex immunostained to reveal cell structures, cell type markers, and analytes, and imaged using multi-spectral microscopy. The image data are processed using novel software that automatically delineates and types each cell in the field, measures morphological features, and quantifies analytes in different sub-cellular compartments of specified cells.

**Results:** The methodology was validated using cell blocks composed of differentially labeled cultured cells mixed in known proportions, and evaluated on human breast carcinoma specimens for quantifying HER2, ER, PR, Ki67, p-ERK and p-S6. Automated cell-level analyses closely matched human assessments, but predictably differed from pixel-level analyses of the same images.

**Conclusions:** Our method reveals the type, distribution, morphology, and biomarker state of each cell in the field, and allows multiple biomarkers to be quantified over specified cell-types, regardless of abundance. It is ideal for studying specimens from patients in clinical trials of targeted therapeutic agents, for investigating minority stromal cell subpopulations, and phenotypic characterization to personalize therapy and prognosis.

## INTRODUCTION

Histopathologic evaluation of tissue samples is indispensable for cancer diagnosis, classification, and management (1, 2), and is an important tool in animal-based research (3, 4). Thin tissue sections are stained with hematoxylin, eosin and/or other chemical stains to reveal cell and tissue structures. Antibody staining to reveal specific molecular biomarkers is increasingly used to improve cancer diagnosis and classification, establish prognosis, and determine therapy. Even as molecular biomarkers play a growing role, the scoring of stained specimens remains largely a visual and subjective process: Cells are coarsely scored as positive or negative or graded for degree of antigen staining, the percentage of positive cells is estimated visually, and overall scores are arbitrarily binned/scaled. This process requires considerable expertise and is susceptible to inter-observer variability, despite standardization efforts (5-13). The use of rough composite score scales

(e.g. 0, 1+, 2+, 3+ staining) is tacit acknowledgement of the inherent imprecision and subjectivity involved.

Recently, computer-automated methods have been developed to quantify antigen expression in tissue images (14-17), offering objectivity, reproducibility, and quantification on a continuous scale. Most operate by measuring the number of pixels stained for one or more antigen and quantifying co-localization of stains. They quantify at the level of individual pixels, groups of pixels or image regions however, and not at the level of individual cells, which are the fundamental units at which many biological processes occur. This is largely due to the lack of sufficiently reliable automated methods to segment (delineate) individual cells, identify subcellular compartments within cells, and quantify biomarkers within the subcellular regions. We set forth an approach that leverages recent advances in imaging, image analysis, and pattern theory to enable biomarkers to be analyzed and quantified on a cell-by-cell basis, providing additional data that cannot be obtained by pixel-level analysis and advancing prior efforts (18) (19). Our segmentation algorithms are capable of delineating sub-cellular compartments using image cues and geometric constraints. The subcellular compartment segmentations are consistently linked, enabling correct analysis in situations that challenge pixel-level analytical methods, e.g., multiple markers that are not co-localized but are present in the same cell. Importantly, our method explicitly identifies cell types, permitting selective measurement of biomarker expression in cell sub-populations regardless of their abundance

## RESEARCH DESIGN & METHODS

**Tissue Staining:** De-paraffinized 5  $\mu$ M sections of formalin-fixed, paraffin-embedded human breast tissues were treated with citric acid (pH = 6) for 15min at 90°C prior to staining. Antibodies used for immunostaining included monoclonal mouse anti-human estrogen receptor (ER), anti-human progesterone receptor (PR), anti-human Ki67, anti-epithelial membrane antigen (EMA), rabbit polyclonal anti-HER2 (Dako, Carpinteria, CA), rabbit anti-phospho(p)-ERK, anti-phospho(p)-S6 (Cell Signaling, Danvers, MA), and mouse anti-multi cytokeratin (CK) monoclonal antibodies (Vector laboratories, Burlingame, CA). ER, PR, Ki67, p-ERK and HER2 were detected by immunohistochemistry (IHC) using biotinylated species-specific secondary antibodies, avidin-linked horseradish peroxidase (HRP) (ABC Kit) and 3,3-diaminobenzidine (DAB) or SG blue (Vector laboratories) HRP chromogen substrate. CK, EMA and p-S6 immunostaining were detected by fluorescence using Zenon Alexa Fluor 488 mouse IgG1 labeling (Invitrogen, Carlsbad, CA), fluorescently labeled secondary antibodies (Invitrogen, Carlsbad, CA) or the ABC fluorescence detection kit. After immunostaining, slides were counterstained with hematoxylin.

Individual slides were stained with combinations of the above antibodies to reveal antigens that reported on cell compartments, cell type and molecular analytes in each slide. Multiplex staining protocols were developed to minimize or avoid the opportunity for nonspecific staining by secondary antibodies. Both chromogenic and fluorescent reporters were frequently used on the same slide, and only fluorochromes that could be resolved spectrally were used on the same slide.

**Tissue imaging:** A Nuance® multispectral camera (CRI Inc., Woburn, MA) on a Leica DMRA2 epifluorescence microscope was used to record images at 400 $\times$  magnification, 8 bits/pixel at 10nm wavelength intervals from 420-720 nm in both brightfield and fluorescent modes. Nuance software was used to spectrally unmix the data into distinct channels representing hematoxylin and the individual chromogens and fluorochroms based on their pure spectra.

**Figure 1** shows a sample breast cancer specimen. The brightfield image (panel A) reveals hematoxylin staining. Panel B shows the hematoxylin channel, unmixed using its spectral signature (Panel F), revealing cell nuclei. Such unmixed channels are ideal for automated segmentation because they are monochrome and

often contain only one type of object. Panel C shows the channel corresponding to CK fluorescent staining, which reveals the cytoplasmic domain of cells of epithelial origin. Panel D shows the channel corresponding to HER2 fluorescent staining, which reveals the plasma membrane of breast cancer cells expressing this biomarker. We use this image as a running example to illustrate the segmentation methods and process.

**Image Analysis Overview:** Our segmentation strategy focuses on cells whose nuclei are visible in the nuclear channel since they mark individual cells – these are segmented first. Second, the cytosolic boundaries of cells whose nuclei are detected are segmented based on markers and geometric constraints. The third step quantifies cell and nuclear morphologies, and measures biomarker expression over cellular compartments. Using these data, we identify cell types, classify cells as being positive/negative for antigens, and organize the measurements by cell type and sub-cellular compartment.

**1. Automated Segmentation of Cell Nuclei:** We used our fully automated segmentation algorithm (20) that improves upon the prior literature (21-35). Importantly, it is capable of automatic selection of parameter settings. It starts by binarizing the image using the Graph-Cuts method with automatic learning of foreground and background intensity profiles using minimum error thresholding (36, 37). Next, a multi-scale Laplacian of Gaussian (LoG) filter, with automatic and adaptive scale selection(20) is used to identify nuclear centers. These points are used to generate an initial segmentation (38) that is refined using a multi-label graph-cuts algorithm with alpha-expansions(39) and graph-coloring (40). **Figure 2A** shows sample automated segmentation results for the image in **Figure 1** as red outlines overlaid on the nuclear channel displayed in grayscale. The green dots indicate nuclear centers whose locations and identifications (IDs) are used in subsequent steps. Given the importance of this step, the user is provided with graphical tools to inspect the results and correct any errors before proceeding to the next step.

**2. Automated Delineation of Cytoplasmic Domains:** This step generates the spatial mask for associating cytoplasmic markers to individual cells using a mix of cues from cytoplasmic and membrane markers and geometric constraints. For example, cytokeratins (CK) are found in the intra-cytoplasmic cytoskeleton of cells of epithelial origin (e.g., carcinoma cells in **Figure 1C**), so they indicate cytoplasmic domains of a selected cell population. Cytoplasmic markers often highlight connected multi-cellular clusters that must be sub-delineated into individual cells to permit cell-by-cell analysis. The cues for this sub-



delineation vary. Sometimes, it is possible to highlight cell boundaries by staining for a membrane-associated antigen, e.g., E-cadherin or EMA. Some analytes also can highlight membranes of cells, e.g. HER2 (**Figure 2D**). However, membrane labeling is often unreliable: HER2 is not always over expressed, and E-cadherin expression can be lost in some cancers. Even when good cytoplasmic and membrane-bound markers are available, some ambiguities arise due to the fact that histopathology slides are sections of three-dimensional (3-D) specimens, and the sectioning plane cannot be planned accurately. For instance, the membranes of cells may be visible but not the nuclei, or the membrane signal can appear over a nucleus, appearing to cut across it. Finally, cells within a sample can show a variable degree of staining. Overall, cytoplasmic segmentation algorithms must be capable of coping with variable cues. Our strategy is to avoid direct segmentation of the cytoplasmic/membrane channels. Instead, we leverage the validated nuclear segmentations and build an adaptive algorithm that exploits cues in the cytoplasmic and/or membrane channels, when they are available, and that defaults to geometric constraints when they are inadequate. It automatically switches between two modes (defined below) on a cell-by-cell basis.

**Mode 0:** This applies to cells with detectable cytoplasmic and/or membrane marker. The cytoplasmic channel pixels  $I_C(x, y)$  are automatically and adaptively binarized to separate the foreground and background, using the Graph-Cuts algorithm (36, 37). Morphological opening and closing operators (radius = 3 pixels) are used to fill holes. If the membrane channel,  $I_M(x, y)$  is available, the magnitude of its smoothed intensity gradient,  $G_\sigma(x, y) = |\nabla_\sigma I_M(x, y)|$  is computed by convolving  $I_M(x, y)$  with the derivative of a Gaussian with  $\sigma = 1.25$  pixels (fixed for a given magnification). If the membrane channel is unavailable, we compute  $G_\sigma(x, y) = |\nabla_\sigma I_C(x, y)|$  instead. The cues from the cytoplasmic and membrane channels are integrated with geometric distances by computing a gradient-enhanced distance map  $S(x, y)$ , with respect to the segmented nuclei. This is used to compare the cue-adjusted proximity of each pixel to nuclei. If  $d(i, j)$  denotes the Euclidean distance between neighboring foreground pixels  $i = (x_i, y_i)$  and  $j = (x_j, y_j)$ , the adjusted distance between them is  $d(i, j) \times |G_\sigma(x_i, y_i) - G_\sigma(x_j, y_j)|$ . The adjusted distance between non-neighboring points  $u_1 = (x_1, y_1)$  and  $u_n = (x_n, y_n)$  is weighted by the length of the

shortest path (with 8-neighbor connectivity) connecting them. The value at each cytoplasmic foreground point in  $S(x, y)$  is set to the minimum of all the adjusted distances from  $(x_F, y_F)$  to all the nuclear boundary points that are connected by a path over foreground points. Using the nuclei as the initial markers, a marker-controlled watershed transform (41) is computed on  $S(x, y)$ . This produces a reliable segmentation of the cytoplasmic foreground into sub-regions, with one cytoplasmic region per segmented nucleus. **Figure 2B** shows sample cell segmentations of CK+ cells using Mode 0 using the gradient information  $G_\sigma(x, y)$  from the membrane channel. **Figures (3, 5, 6 and supplementary Figure 2)** exemplify segmentations without the benefit of the membrane signal.

**Mode 1:** This is a geometric estimation that is invoked for cells for which cytoplasmic and membrane labels are unavailable (e.g., stromal cells that are CK-). The traditional geometric approach based on Voronoi diagrams(42, 43) produces unacceptably coarse polygonal approximations, so we use the Hamilton-Jacobi Generalized Voronoi Diagram (HJ-GVD) (44) that uses the Euclidean distance from segmented nuclear boundaries instead of their centroids to produce more refined estimates. We impose a radius constraint  $r_{\max}$  on the HJ-GVD to prevent unrealistically large cell domain estimates. **Figure 2C** shows sample results for the HER2 example using  $r_{\max} = 12$  pixels. The estimated cell boundaries are overlaid on the Euclidean distance map  $D(x, y)$ . Although these geometric estimates do not reflect the cellular reality (the structures are unobservable), they are helpful for approximately associating extranuclear markers to cells when the limitations of immunostaining do not permit additional labels for cytoplasmic & membrane markers.

**3. Morphological Measurements of Cells:** From the nuclear and cytoplasmic segmentations, we compute cell features including locations, areas, shape factors, boundary curvatures, convexity, eccentricity, radius variation, orientation, and various texture measures (average intensity, intensity variation, skew of intensity distribution, energy of intensity distribution, entropy of intensity distribution, interior gradient, and ratios of intensity values (e.g., max/min)) (45). Not all features are needed for a given analysis, and the user can choose an appropriate subset. The cytoplasmic segmentation step produces one cytoplasmic domain per segmented nucleus, so the nuclear identifiers (IDs) are used for tabulating nuclear and cytoplasmic measurements.

4. **Biomarker Measurements of Cells** Next, molecular biomarkers are quantified by measuring their distribution over cellular regions of interest (masks) defined by segmentation. **Figure 2E** shows a close-up view of these regions for an individual cell. The red outline shows the intranuclear compartment, the light blue contours delineate the intra-cytoplasmic compartment, and the orange contour runs parallel to the cell membrane outline (blue) separated by a fixed distance (5 pixels).

**Quantifying Nuclear Biomarkers:** Directly summing the analyte signal over intranuclear compartments is naïve since it does not correct for background fluorescence. Even when they appear dim, background pixels can add up to a significant sum over a region. To address this problem, we first perform an automatic 2 or 3-level segmentation of the analyte channel(46). When the contrast between the analyte-positive pixels and analyte-negative pixels is high, a 2-level binarization separates the bright foreground from definite background pixels. When the analyte exhibits an intermediate background, a 3-level binarization (e.g., **Figure 4**) segregates pixels into bright foreground, intermediate background, and dark background. Only the bright foreground pixels are used for analyte association. **Supplementary Figure 3** illustrates these steps for quantifying ER in a breast cancer specimen. Panel D shows the 3-level binarization for background correction.

**Quantifying Cytoplasmic Markers:** Integration of markers over the cytoplasmic region proceeds as with nuclei – the background-corrected analyte signal is integrated over the cytoplasmic region of interest. In **Figure 2E**, the cytoplasmic region of integration is enclosed by the blue outlines, but excluding the intranuclear region.

**Quantifying Plasma Membrane Bound Markers:** This computation must cope with the possibility of an unreliable membrane label that does not clearly and completely define the cytoplasmic domain of each cell. Happily, our cytoplasmic segmentation is designed to produce closed contours representing the best-possible estimates of cell membrane locations based on available cues. When a user determines that the membrane signal is sufficiently reliable, membrane-bound analytes can be integrated within a narrow strip (typ. 5 pixels wide) of the segmented membrane. When the locations of cytoplasm and plasma membrane markers are superimposed or extensively overlap, the integration is carried out over the entire cell domain, with background correction. The resulting biomarker measurements must be interpreted with care, since our

images represent planar projections of sub-cellular compartments with finite thickness. When assigning analyte expression to sub-cellular compartments, one must acknowledge that these two compartments cannot be perfectly distinguished or separated in the images being analyzed. Nevertheless, these measurements are adequate from the standpoint of labeling cells as being positive/negative for membrane bound antigens, and for statistical analysis.

**5. Cell Type Identification:** This step identifies whether a cell is of a specified type based on its morphological and associative features. We use a supervised approach, where a training set (containing examples of both classes from one or more images) is indicated by the user, from which a Bayesian classifier is constructed. **Figure 2D** illustrates cell classification results for the example image shown in **Figure 1**, based on the cytokeratin signal. Yellow dots represent cells that are CK+ and HER2+, and white dots represent other cells.

## EXPERIMENTAL RESULTS

FARSIGHT ([www.farsight-toolkit.org](http://www.farsight-toolkit.org)) was written using standard software tools (C++, ITK, VTK, QT) and allows a user to perform automated segmentation, view & edit the results, compute morphological & associative features, classify cells, and export the results to spreadsheets. It is both free and open source. Each row of the output corresponds to one numbered cell in the image. The software was validated in two ways. First, its results were compared against determinations made by a human expert. Another validation was based on in vitro cultured cells, labeled with different fluorochromes and mixed in different ratios to create cell blocks from which slides were cut for fluorescence imaging and analysis. Specifically, cultured cells were labeled with the membrane dye, PKH26, or with a combination of PKH26 and PKH67. The PKH26 cells and PKH26/PKH67 cells were mixed in different ratios (10:0, 9:1, 2:1, 1:1, 1:2, 1:9 and 0:10), fixed and frozen in OCT embedding media. Slides cut from these cell blocks were stained with DAPI to reveal nuclei and membrane proteins PKH26 and PKH67. The details of the protocols and results are in **Supplement A**. Ten images (400X) were taken of slides from each block and processed by FARSIGHT to segment cells, classify them as PKH67-negative or PKH67-positive, and compute the ratio of the two cell populations. The results were in concordance with a human expert scoring (Table A.1). The averages of cell

proportions determined by FARSIGHT closely approximated the known truth (Supplementary Figure A.1). We then proceeded to evaluate FARSIGHT for human breast histopathology samples.

**Cell membrane Analyte (HER2):** **Figure 2** shows our analysis of the image in **Figure 1**. The histogram in **Figure 2F** shows the distribution of HER2 in the cells. The cut-off value was 12.6 grayscale units, at which 98.5% of the tumor cells (CK+ cells) are HER2+. These data concord with an expert human reading of 99%. In some cases, HER2 staining is not also usable for cell boundary determination (e.g. HER2 staining overlays cell nuclei or is extremely dark and thick (**Supplementary Figure 1**), so the cell boundaries were estimated geometrically (Mode 1).

**Nuclear Analytes (ER, PR, Ki67):** We applied our methodology to specimens stained for 3 common nuclear-bound markers, ER, PR and Ki67. **Supplementary Figure 2** shows the detailed steps for the ER case – the steps were identical for PR and Ki67. **Figure 3** shows the results for breast cancer specimens stained for ER (A, B), PR (C, D), and Ki67 (E, F), respectively. As a crosscheck, we computed the ratios of nuclear to cytoplasmic levels of the analytes for every cell. Histograms of these ratios (panels B, D, F) show that these analytes are strongly nuclear bound, as expected for antigens that are located in nuclei. The automatically determined percentages of ER+, PR+ and Ki67+ cells were 39%, 40% and 27% of the CK+ cells, compared to expert determined percentages of 38%, 39% and 26%, respectively. For comparison, pixel-level analysis to determine the percentage of hematoxylin+ pixels (the image area occupied by nuclei) that were also ER+, PR+ or Ki67+ yielded 17.3%, 28.5% and 14.5%, respectively. Clearly, area measurements do not reflect cell numbers.

**Figure 4** illustrates analysis of chosen sub-populations of cells. To measure cell proliferation and its relationship to activity of the Raf-MEK-ERK signaling pathway, a human breast carcinoma was immunostained for Ki67, p-ERK and CK. CK staining reveals a cluster of carcinoma cells to the right, but these constitute a minority of the cells; the majority are lymphocytes within a reactive lymphoid nodule. Ki67 immunostaining showed that 34.6% of all cells were proliferating. For comparison, pixel-level analysis showed that 16.7% of hematoxylin+ pixels were Ki67+. Only 2.1% (2 of 96) of carcinoma cells are Ki67+, while 37.8% (414 of 1094 stromal cells) are Ki67+. Thus the total number or percentage of Ki67+ cells does not accurately report tumour cell proliferative activity. It demonstrates that a cell-based method with the

ability to type cells as tumour or stromal prior to analyte quantification is important for characterizing human tumours, where the cellular composition is always heterogeneous, and tumour cells may not predominate. Further analysis to examine the correlation between Raf-MEK-ERK signaling and proliferation showed a high coefficient ( $R = 0.89$ ) between p-ERK and Ki67 expression in cells (**Figure 4E**). It suggests that ERK activation and proliferation may be linked events among the cells in this image. This is expected, since the majority of proliferating cells are lymphocytes, and ERK activation has been shown to accompany mitogenic activation of lymphocytes *in vitro* (47). Due to the low frequency of Ki67 and p-ERK positivity among CK+ cells in this image, little can be learned about concurrence of ERK activation and proliferation in carcinoma cells from this image (**Figure 4F**).

To examine the relationship between ERK activation and proliferation in breast cancer cells, another region of the same tumour (**Figure 5A-C**) and a region of a second, similarly stained tumour (**Figure 5G-I**) were analyzed. In both fields, tumor cells are the majority, and a significant fraction are Ki67+ (10% for tumour 1, 7.5% for tumour 2). Scatter plots of p-ERK and Ki67 expression in individual cells reveal that the correlation between p-ERK and Ki67 staining is less among the CK+ carcinoma cells of tumour 1 ( $R = 0.59$ ) and tumour 2 ( $R = 0.29$ ) than among the reactive lymphocytes in tumour 1 (**Figure 4**,  $R = 0.89$ ). Based on these images, the link between ERK activation and cell proliferation appears weaker in the tumour cells than in the reactive lymphocytes, illustrating the utility of specific cell-level analysis as a research tool.

The ability of our method to separate each cell into nuclear and extranuclear compartments is valuable. **Figure 6** shows a breast tumour that was stained with antibodies to p-S6 (the activated form of ribosomal protein S6), CK and EMA, all by immunofluorescence, and counterstained with hematoxylin. **Figure 6D** shows cell segmentation and classification results with yellow contours outlining the cytoplasmic boundaries of CK+ cells determined using the CK and EMA channels jointly. The sub-population of CK+ cells that are p-S6+ is in the minority (11%) in this tumour (for comparison, pixel based analysis showed that 8.9% of CK+ pixels are p-S6+). Visual examination of the p-S6+ cells shows that p-S6 staining, as expected, was predominantly cytoplasmic. This was confirmed by plotting a histogram of the extra-nuclear to nuclear ratio of p-S6 signal in cells that expressed this antigen (**Figure 6F**), which showed that only 10% of p-S6 signal was nuclear. This small amount of “nuclear” p-S6 may be explained by the fact that the image represents a

planar projection of a tumour section that is 5µm thick; p-S6 staining in cell cytoplasm situated above or below nuclei in these sections would register as nuclear.

## **DISCUSSION & CONCLUSIONS**

The “histocytometric” analyses performed by FARSIGHT on the images shown demonstrate the practicality and value of quantifying molecular analytes on a cellular scale with cell-type and sub-cellular compartment specificity. Although these studies focused on breast cancer, our methodology and tools are applicable to other cancers and conditions. Our approach requires more extensive immunostaining and sophisticated imaging compared to traditional visual histopathology, but offers important benefits. It reveals the type, distribution, intrinsic characteristics and biomarker state of each cell in its tissue context. It allows multiple biomarkers to be quantified selectively over specified cell-types, regardless of their abundance. Our efforts were focused on quantifying analytes in tumor cells, but stromal cells (endothelial cells, fibroblasts, lymphocytes, macrophages, etc.) are omnipresent in tumors and gaining attention for their contributions to malignant progression and behavior (48) (49). The ability of histocytometry to specify the cell-type for analysis makes it a sensitive and specific tool for investigating minority stromal cell subpopulations, whose attributes would otherwise be overshadowed by more abundant cell types.

Our cell-based method shares some advantages with pixel-level analysis, such as objectivity, reproducibility, and ability to quantify on a continuous scale. However, by using the cell as the unit of analysis, it generates additional and potentially complementary measurements expressible in terms of cell counts and cell types. Such measurements are unaffected by the area occupied by cells and other tissue structures in the image. While the two types of measurements can be correlated for some samples, they can differ greatly for others, as shown by our examples. For analysis of histopathology specimens, both methods are usable diagnostically, but we believe that event reporting by cell number or percentage is biologically more informative, as reflected in the fact that it is the preferred form of reporting for many *in vitro* cellular studies. Our software system makes it possible to generate these reports.

Histocytometry correctly assigns analytes to appropriate subcellular locations within one cell (e.g. a nuclear analyte and a cytoplasmic analyte) to the same unit. Results so organized have obvious benefits,

particularly when interrogating tissues for biological processes and events that occur, or are regulated, at the level of individual cells but involve different subcellular compartments. This feature of FARSIGHT analysis also brings the ability to examine and quantify analytes in different compartments of cells. This is an advantage when studying analytes whose subcellular location, by itself, is informative about activity. For example, the transcription factor, NF $\kappa$ B, is kept transcriptionally inactive when it is constrained in the cytoplasm through binding to its inhibitor, I $\kappa$ B. NF $\kappa$ B becomes active upon its translocation to the nucleus following stimuli that induce release from and degradation of I $\kappa$ B (50). An extension of this is the study of yet other analytes that produce different effects, depending on whether they are localized to the cytoplasm or nucleus. Finally, by providing analyte data for each cell in an image rather than one result for the image as a whole, FARSIGHT analysis can reveal population characteristics, such as analyte range, distribution, and variance among cells that can be additionally informative. Histocytometry can provide information similar to that provided by flow cytometry with the added benefit of preserving tissue architecture, which allows concurrent examination of morphological features and quantification of spatial relationships and distributions not possible with the dissociated cells used for flow cytometry.

We developed our multiplex immunostaining protocols for the study of formalin-fixed, paraffin-embedded (FFPE) histopathology specimens. This allows histocytometric analysis to be performed on the tissue material most commonly available from cancer patients and most often stored in pathology archives. However, frozen and other forms of preserved tissues are also suitable for this type of analysis; their study only requires development of appropriate immunostaining protocols. These protocols have involved immunostaining for four or more antigens on the same slide to study a single analyte. This level of complexity stems from the need to stain for cell type, subcellular compartments, and analyte antigens on the same slide. Some of this complexity may be reduced by algorithms for direct multi-spectral identification of tumor cells and tumor areas in slides stained only with hematoxylin and eosin (H&E). For tumor cell analysis, computer generated “tumor masks” may eliminate the need to immunostain for cell type and compartment antigens. Combining use of tumor masks with cell segmentation based on geometric algorithms, histocytometry analysis may be performed on slides stained only for analyte and H&E, such as breast cancer specimens stained for ER, PR and HER2 in hospital pathology laboratories. While the utility



of developing methods for histocytometric analysis of simply stained slides is primarily clinical, expanding the current limits of immunostain multiplexing will make histocytometry an even more potent instrument for biology research. FARSIGHT can also be applied to H&E stained sections, but the caveat rests with the fluorescence of eosin that must be properly accounted for in the spectral unmixing. It will allow study of numerous analytes on the same slide. Accompanied by FARSIGHT cell-based quantification of their expression, this will enable examination of complex patterns of signaling pathway activity and other molecular events in cells in authentic tissue context. Although our examples did not show analysis of multiple cell types, the system itself is capable of such analysis and we expect to report validation of this capability in subsequent papers. As part of our effort to hasten development and advancement of this histopathology analysis platform, FARSIGHT has been made available as a free & open source software system ([www.farsight-toolkit.org](http://www.farsight-toolkit.org)). In the future, we expect this system to be adapted to automated analysis of larger batches of specimens, that may be multiplex stained by automated systems, and whole-slide scanning.

## REFERENCES

1. Cheng J, Qiu S, Raju U, Wolman SR, Worsham MJ. Benign breast disease heterogeneity: association with histopathology, age, and ethnicity. *Breast Cancer Res Treat* 2008 Sep; 111(2): 289-96.
2. Hammerschmied CG, Walter B, Hartmann A. [Renal cell carcinoma 2008 : Histopathology, molecular genetics and new therapeutic options.]. *Pathologie* 2008 Sep; 29(5): 354-63.
3. Crocker J, Murray P. *Molecular biology in cellular pathology*, John Wiley & Sons: Chichester, West Sussex, England ; Hoboken, NJ, 2003, xx, 380 p.pp.
4. Research Signpost (Trivandrum India). Recent research developments in histopathology. Research Signpost: Trivandrum, India; 2002. p v.
5. Menard S, Balsari A, Tagliabue E, *et al.* Biology, prognosis and response to therapy of breast carcinomas according to HER2 score. *Ann Oncol* 2008 Oct; 19(10): 1706-12.
6. Chivukula M, Bhargava R, Brufsky A, Surti U, Dabbs DJ. Clinical importance of HER2 immunohistologic heterogeneous expression in core-needle biopsies vs resection specimens for equivocal (immunohistochemical score 2+) cases. *Mod Pathol* 2008 Apr; 21(4): 363-8.
7. Montironi R, Mazzucchelli R, Barbisan F, *et al.* HER2 expression and gene amplification in pT2a Gleason score 6 prostate cancer incidentally detected in cystoprostatectomies: comparison with clinically detected androgen-dependent and androgen-independent cancer. *Hum Pathol* 2006 Sep; 37(9): 1137-44.

8. Bowles DW, Rabinovitch R, Borges V, *et al.* A young woman with a small ER-positive breast cancer, a micrometastatic axillary lymph node, and an intermediate oncotype DX recurrence score. *Oncology (Williston Park)* 2007 Sep; 21(10): 1212-7.
9. Remmele W, Stegner HE. [Recommendation for uniform definition of an immunoreactive score (IRS) for immunohistochemical estrogen receptor detection (ER-ICA) in breast cancer tissue]. *Pathologe* 1987 May; 8(3): 138-40.
10. Neudert M, Fischer C, Krempien B, Seibel MJ, Bauss F. A rapid histological score for the semiquantitative assessment of bone metastases in experimental models of breast cancer. *Onkologie* 2008 Oct; 31(10): 521-7.
11. Egyed Z, Jaray B, Kulka J, Pentek Z. Triple Test Score for the Evaluation of Invasive Ductal and Lobular Breast Cancer. *Pathol Oncol Res* 2008 Aug 28.
12. Kurosumi M. Immunohistochemical assessment of hormone receptor status using a new scoring system (J-Score) in breast cancer. *Breast Cancer* 2007; 14(2): 189-93.
13. Remmele W, Schickelanz KH. Immunohistochemical determination of estrogen and progesterone receptor content in human breast cancer. Computer-assisted image analysis (QIC score) vs. subjective grading (IRS). *Pathol Res Pract* 1993 Sep; 189(8): 862-6.
14. Camp RL, Chung GG, Rimm DL. Automated subcellular localization and quantification of protein expression in tissue microarrays. *Nat Med* 2002 Nov; 8(11): 1323-7.
15. Mulrane L, Rexhepaj E, Penney S, Callanan JJ, Gallagher WM. Automated image analysis in histopathology: a valuable tool in medical diagnostics. *Expert Rev Mol Diagn* 2008 Nov; 8(6): 707-25.
16. Taylor CR, Levenson RM. Quantification of immunohistochemistry--issues concerning methods, utility and semiquantitative assessment II. *Histopathology* 2006 Oct; 49(4): 411-24.
17. Tamai S. [Expert systems and automatic diagnostic systems in histopathology--a review]. *Rinsho Byori* 1999 Feb; 47(2): 126-31.
18. Peterson RA, Krull DL, Butler L. Applications of laser scanning cytometry in immunohistochemistry and routine histopathology. *Toxicol Pathol* 2008; 36(1): 117-32.
19. Davis DW, Takamori R, Raut CP, *et al.* Pharmacodynamic analysis of target inhibition and endothelial cell death in tumors treated with the vascular endothelial growth factor receptor antagonists SU5416 or SU6668. *Clin Cancer Res* 2005 Jan 15; 11(2 Pt 1): 678-89.
20. Al-Kofahi Y, Lassoued W, Lee W, Roysam B. Improved Automatic Detection & Segmentation of Cell Nuclei in Histopathology Images. *IEEE Trans Biomed Eng* 2009((in review)).
21. Chang H, Yang Q, Parvin B. Segmentation of heterogeneous blob objects through voting and level set formulation. *Pattern Recognition Letters* 2007 Oct 1; 28(13): 1781-7.
22. Parvin B, Yang Q, Han J, *et al.* Iterative voting for inference of structural saliency and characterization of subcellular events. *Ieee Transactions on Image Processing* 2007 Mar; 16(3): 615-23.
23. Wahlby C, Sintorn IM, Erlandsson F, Borgefors G, Bengtsson E. Combining intensity, edge and shape information for 2D and 3D segmentation of cell nuclei in tissue sections. *Journal of Microscopy-Oxford* 2004 Jul; 215: 67-76.

24. Ortiz de Solorzano C, Garcia Rodriguez E, Jones A, *et al.* Segmentation of confocal microscope images of cell nuclei in thick tissue sections. *J Microsc* 1999 Mar; 193(Pt 3): 212-26.
25. Lin G, Chawla MK, Olson K, *et al.* A multi-model approach to simultaneous segmentation and classification of heterogeneous populations of cell nuclei in 3D confocal microscope images. *Cytometry A* 2007 Sep; 71(9): 724-36.
26. Lin G, Chawla MK, Olson K, *et al.* Hierarchical, model-based merging of multiple fragments for improved three-dimensional segmentation of nuclei. *Cytometry A* 2005; 63(1): 20-33.
27. Mackin RW, Jr., Newton LM, Turner JN, Holmes TJ, Roysam B. Accuracy of nuclear classification in cervical smear images. Quantitative impact of computational deconvolution and 3-D feature computation. *Anal Quant Cytol Histol* 1998 Apr; 20(2): 77-91.
28. Mackin RW, Jr., Newton LM, Turner JN, Roysam B. Advances in high-speed, three-dimensional imaging and automated segmentation algorithms for thick and overlapped clusters in cytologic preparations. Application to cervical smears. *Anal Quant Cytol Histol* 1998 Apr; 20(2): 105-21.
29. Ancin H, Roysam B, Dufresne TE, *et al.* Advances in automated 3-D image analyses of cell populations imaged by confocal microscopy. *Cytometry* 1996 Nov 1; 25(3): 221-34.
30. Byun JY, Verardo MR, Sumengen B, *et al.* Automated tool for the detection of cell nuclei in digital microscopic images: Application to retinal images. *Molecular Vision* 2006 Aug 16; 12(105-07): 949-60.
31. Chawla MK, Lin G, Olson K, *et al.* 3D-catFISH: a system for automated quantitative three-dimensional compartmental analysis of temporal gene transcription activity imaged by fluorescence in situ hybridization. *J Neurosci Methods* 2004 Oct 15; 139(1): 13-24.
32. De Solorzano CO, Malladi R, Lelievre SA, Lockett SJ. Segmentation of nuclei and cells using membrane related protein markers. *Journal of Microscopy-Oxford* 2001 Mar; 201: 404-15.
33. Gudla PR, Nandy K, Collins J, *et al.* A high-throughput system for segmenting nuclei using multiscale techniques. *Cytometry A* 2008 May; 73(5): 451-66.
34. Li G, Liu TM, Nie JX, *et al.* Detection of blob objects in microscopic zebrafish images based on gradient vector diffusion. *Cytometry Part A* 2007 Oct; 71A(10): 835-45.
35. Lin G, Adiga U, Olson K, *et al.* A hybrid 3D watershed algorithm incorporating gradient cues and object models for automatic segmentation of nuclei in confocal image stacks. *Cytometry A* 2003 Nov; 56(1): 23-36.
36. Kittler J, Illingworth J. Minimum Error Thresholding. *Pattern Recognition* 1986; 19(1): 41-7.
37. Pal NR, Pal SK. Image model, Poisson distribution and object extraction. *International Journal of Pattern Recognition and Artificial Intelligence* 1991; 5(3): 25.
38. Wu XW, Chen YD, Brooks BR, Su YA. The local maximum clustering method and its application in microarray gene expression data analysis. *Eurasip Journal on Applied Signal Processing* 2004 Jan 1; 2004(1): 53-63.
39. Boykov Y, Veksler O, Zabih R. Fast approximate energy minimization via graph cuts. *IEEE Transactions on Pattern Analysis and Machine Intelligence* 2001 Nov; 23(11): 1222-39.

40. Nath SK, Bunyak F, Palaniappan K. Robust Tracking of Migrating Cells Using Four-Color Level Set Segmentation. *Lect Notes Comput Sci* 2006; 4179(LNCS): 920-32.
41. Vincent L, Soille P. Watersheds in Digital Spaces - an Efficient Algorithm Based on Immersion Simulations. *IEEE Transactions on Pattern Analysis and Machine Intelligence* 1991 Jun; 13(6): 583-98.
42. Bertin E, Parazza F, Chassery JM. Segmentation and measurement based on 3D Voronoi diagram: application to confocal microscopy. *Comput Med Imaging Graph* 1993 May-Jun; 17(3): 175-82.
43. Sanchez-Marin FJ. A simple procedure for simulating samples of tissue using Voronoi diagrams. *Anal Quant Cytol Histol* 2005 Aug; 27(4): 225-31.
44. Nath SK, Palaniappan K, Bunyak F. Accurate Spatial Neighborhood Relationships for Arbitrarily-shaped Objects using Hamilton-Jacobi GVD. *Lect Notes Comput Sci* 2007; 4522 LNCS: 421-31.
45. Bjornsson CS, Lin G, Al-Kofahi Y, *et al.* Associative image analysis: a method for automated quantification of 3D multi-parameter images of brain tissue. *J Neurosci Methods* 2008 May 15; 170(1): 165-78.
46. Al-Kofahi Y, Lassoued W, Lee W, Roysam B. Improved Automatic Detection & Segmentation of Cell Nuclei in Histopathology Images. *IEEE Trans Biomed Eng* 2009 Oct 30.
47. Cantrell D. T cell antigen receptor signal transduction pathways. *Annu Rev Immunol* 1996; 14: 259-74.
48. Kerbel RS. Tumor angiogenesis. *N Engl J Med* 2008 May 8; 358(19): 2039-49.
49. Orimo A, Gupta PB, Sgroi DC, *et al.* Stromal fibroblasts present in invasive human breast carcinomas promote tumor growth and angiogenesis through elevated SDF-1/CXCL12 secretion. *Cell* 2005 May 6; 121(3): 335-48.
50. Baeuerle PA, Baltimore D. I kappa B: a specific inhibitor of the NF-kappa B transcription factor. *Science* 1988 Oct 28; 242(4878): 540-6.

## FIGURE LEGENDS

**Figure 1: Multiplex stained human breast cancer specimen.** A human breast cancer was stained for HER2 by immunofluorescence using Texas red and for cytokeratin by immunofluorescence using Alexa-488 and counterstained with hematoxylin. The slide was imaged multi-spectrally in absorption and fluorescence modes, and the results unmixed to yield non-overlapping channels. (A) Brightfield image showing hematoxylin staining. (B) Unmixed channel containing only cell nuclei, corresponding to the hematoxylin spectral signature. (C) Unmixed channel for fluorescently-stained cytokeratin. (D) Unmixed channel corresponding to fluorescently stained HER2. (E) Composite 3-color image with nuclei (red), cytokeratin (green), and HER2 (blue). (F) Spectral signatures used for the unmixing computations, displayed using blue for hematoxylin (nuclei), green for Alexa-488 (cytokeratin), and red for Texas Red (HER2).

**Figure 2: Automated image analysis steps for the specimen in Figure 1.** (A) Automatic nuclear segmentation (red outlines) of the nuclear channel. (B) Estimated cytoplasmic domains for cytokeratin+ cells for the boxed region in panel D overlaid on the gradient enhanced distance map (Mode 0). (C) Geometrically estimated cytoplasmic domains for stromal cells in the same region overlaid on the underlying dominance map (Mode 1). (D) Composite cell segmentation & classification results, with yellow dots indicating cells that are cytokeratin+ and HER2+, and white dots indicating other cells. (E) Close-up illustrating regions of interest used to quantify HER2. (F) Histogram summary showing the cutoff point for declaring cells HER2+.

**Figure 3: Examples showing analysis of breast cancer specimens stained for three nuclear-bound biomarkers.** Breast cancer slides were immunostained for estrogen receptor (A, B), progesterone receptor (C,D), or Ki67 (E, F) plus cytokeratin and counterstained with hematoxylin. Images were captured, and nuclear and whole cell segmentation was performed, with yellow dots indicating the nuclei positive for the respective analytes (A, C, E). Analyte was quantified in the nuclear and extranuclear compartments of each cell, and histograms of the ratios of nuclear to extranuclear analyte levels in all positive cells are shown (B, D, F).

**Figure 4: Duplex analysis of pERK and Ki67 immunostaining in lymphoid cells in a human breast carcinoma.** A section of a breast tumor was stained sequentially with anti-pERK (SG blue), anti-Ki67 (DAB) and anti-CK (Alexa-488) antibodies, followed by hematoxylin staining, multispectral imaging (400X) and cytometric analysis. The brightfield image of a lymphoid nodule in the tumor is shown (A) along with the unmixed channels for DAB (Ki67) (B), SG blue (p-ERK) (C) and Alexa-488 (cytokeratin) (D). Scatter plots of p-ERK (X-axis) and Ki67 (Y-axis) staining intensity are shown for cells in the lymphoid nodule (E) and for tumor cells (F), with each dot representing one cell.

**Figure 5: Duplex analysis of pERK and Ki67 immunostaining in human breast carcinoma cells.**

Sections of two different breast tumors were stained and analyzed as described for Figure 5. Brightfield images of the two different tumors are shown (A, G), with the unmixed channels for DAB (Ki67) (B,H) and SG blue (p-ERK) (C,I). Composite images showing whole cell segmentation of the tumor (cytokeratin+) cells are shown (D,J). Scatter plots of p-ERK (X-axis) and Ki67 (Y-axis) staining intensity are shown for tumor cells (E,K) and for non-tumor (stromal) cells in (F,L) with each dot representing one cell.

**Figure 6: Analysis of phospho-S6 immunostaining in a human breast cancer.** A section of a breast tumor was stained with anti-p-S6 (Alexa-488), anti-EMA (Alexa-594) and anti-CK (Alexa-555), followed by hematoxylin staining, multispectral imaging (400X) and cytometric analysis. The brightfield image is shown (A) along with unmixed channels for Alexa-555 (CK) (B) and Alexa-594 (EMA) (C). Composite images of p-S6 analyte staining along with segmented whole tumor cells are shown (D; E shows an enlargement of the boxed area in D). In each cell, analyte in the nuclear and extranuclear compartment was quantified. Ratios of extranuclear to nuclear analyte were calculated for each positive tumor cell and their distribution is shown (F).

**Supplementary Figure 1: Illustrating application of the proposed methods to a breast cancer specimen labeled for HER2** and cell nuclei only. The specimen was stained for HER2 by IHC using DAB and counterstained with hematoxylin. (A) Brightfield image of slide showing HER2 staining in DAB (brown chromogen) counterstained with hematoxylin (B) Composite 2-color image with red corresponding to the nuclear channel, and light blue corresponding to the **HER2** channel (C) Combined segmentation and classification results overlaid on the composite image shown in panel B. The bright blue outlines indicate cell boundaries that were estimated using a fixed distance of 10 pixels surrounding cell nuclei, using the method described as Case III. Yellow and pink dots represent **HER2**<sup>+</sup> and **HER2**<sup>-</sup> cells respectively.

**Supplementary Figure 2:** Application of the proposed method to a breast cancer specimen labeled for Estrogen Receptor (ER) by IHC using DAB, and for CK by IF using Alexa-488 and counterstained with hematoxylin. (A) Brightfield image. (B) Composite 3-color image after spectral unmixing with red, green, and blue corresponding to the nuclear, cytokeratin and ER channels respectively. (C) The raw ER channel. (D) Three-level binarization of the ER channel for background correction. (E) Combined segmentation and classification results overlaid on the composite image in panel B. Yellow and pink dots indicate ER<sup>+</sup> and ER<sup>-</sup> cells. (F) Histogram of the background-corrected intra-nuclear ER signal in cell nuclei. The ER density cut-off value between ER<sup>-</sup> and ER<sup>+</sup> is 55.2 and 39% of the tumor cells (CK<sup>+</sup>) are identified as ER<sup>+</sup>. This percentage is very close to the manual estimate, which is 38%.

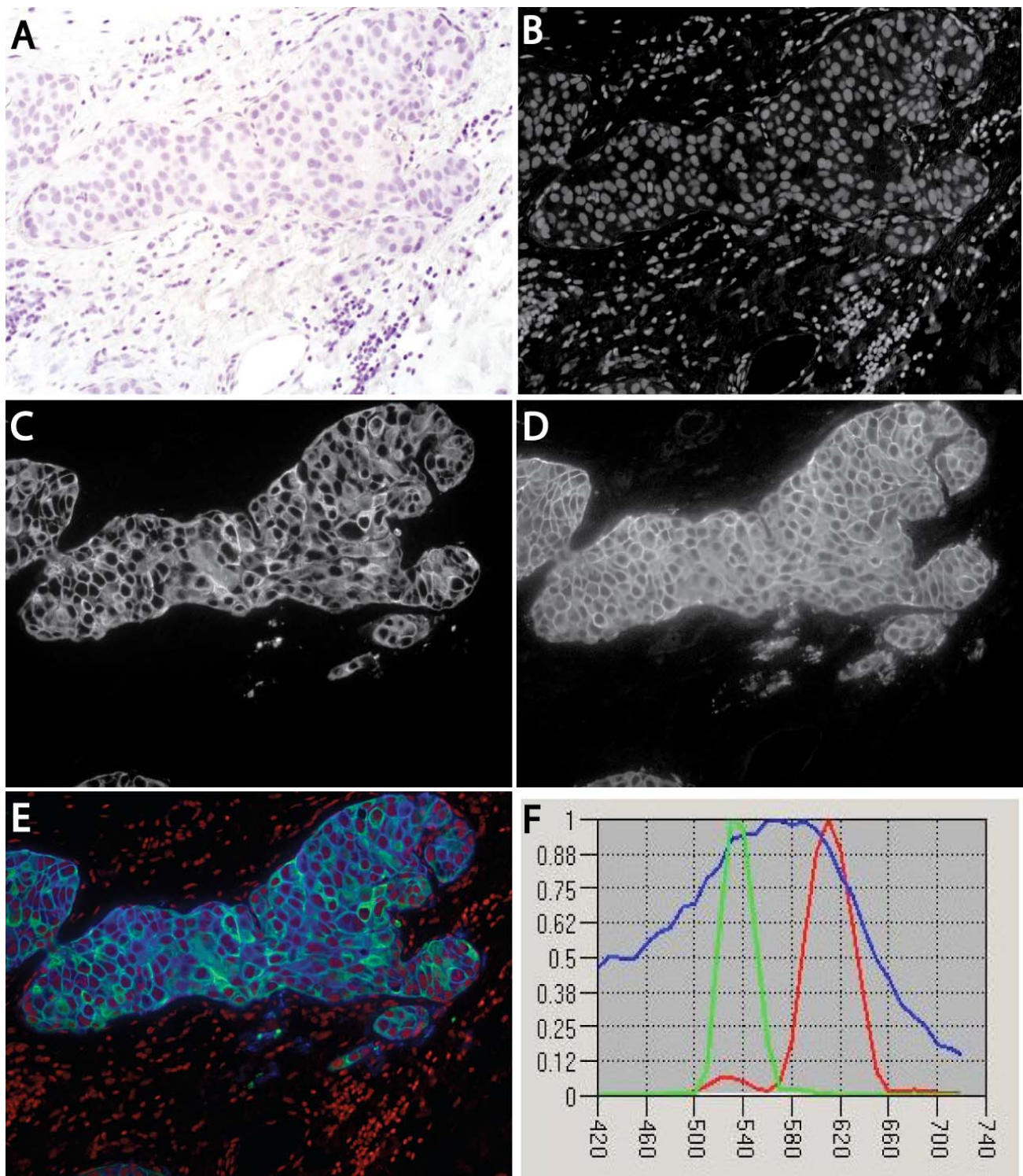


**Figure 1: Multiplex stained human breast cancer specimen.** A human breast cancer was stained for HER2 by immunofluorescence using Texas red and for cytokeratin by immunofluorescence using Alexa-488 and counterstained with hematoxylin. The slide was imaged multi-spectrally in absorption and fluorescence modes, and the results unmixed to yield non-overlapping channels. (A) Brightfield image showing hematoxylin staining. (B) Unmixed channel containing only cell nuclei, corresponding to the hematoxylin spectral signature. (C) Unmixed channel for fluorescently-stained cytokeratin. (D) Unmixed channel corresponding to fluorescently stained HER2. (E) Composite 3-color image with nuclei (red), cytokeratin (green), and HER2 (blue). (F) Spectral signatures used for the unmixing computations, displayed using blue for hematoxylin (nuclei), green for Alexa-488 (cytokeratin), and red for Texas Red (HER2).



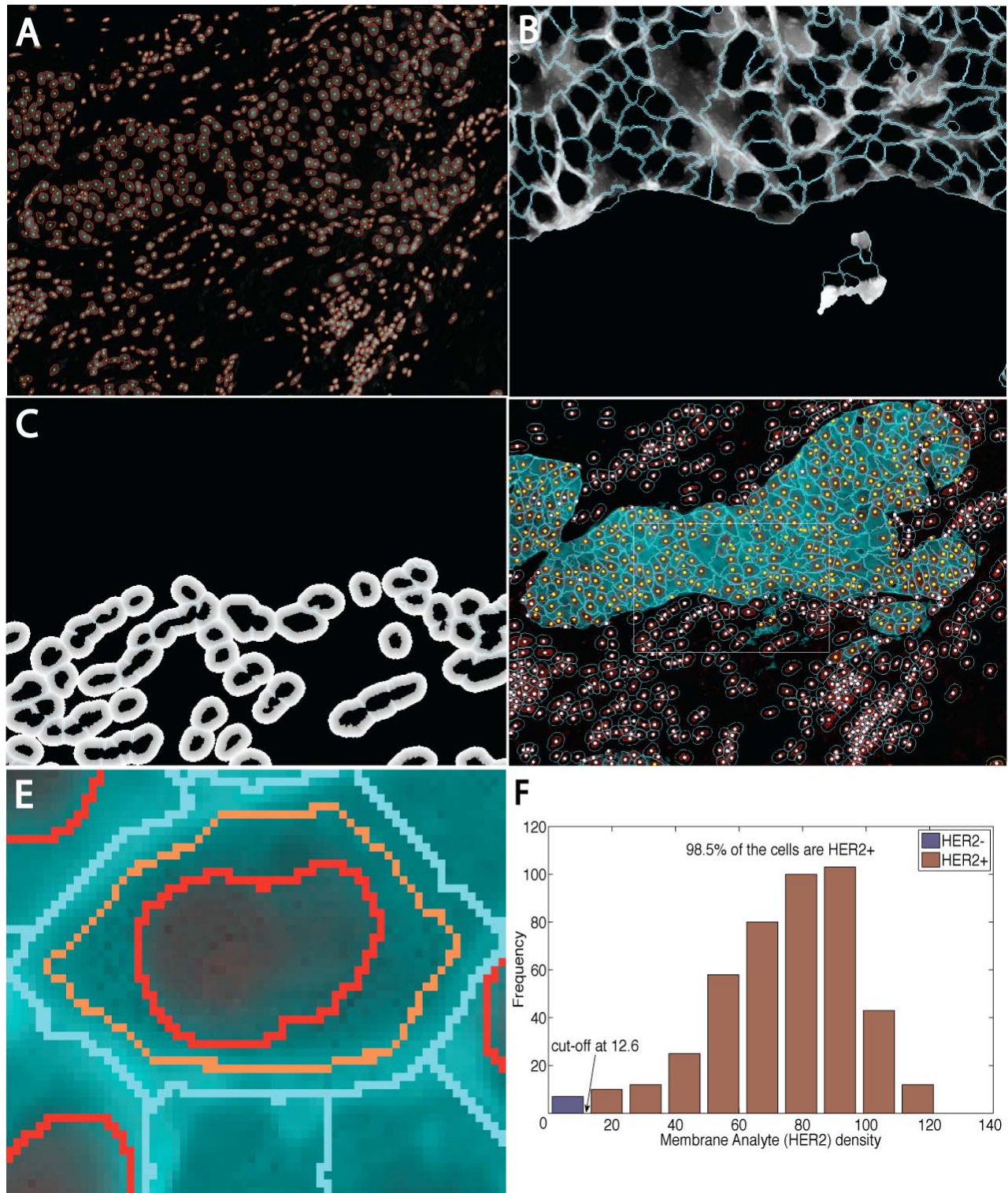


**Figure 2: Automated image analysis steps for the specimen in Figure 1.** (A) Automatic nuclear segmentation (red outlines) of the nuclear channel. (B) Estimated cytoplasmic domains for cytokeratin+ cells for the boxed region in panel D overlaid on the gradient enhanced distance map (Mode 0). (C) Geometrically estimated cytoplasmic domains for stromal cells in the same region overlaid on the underlying dominance map (Mode 1). (D) Composite cell segmentation & classification results, with yellow dots indicating cells that are cytokeratin+ and HER2+, and white dots indicating other cells. (E) Close-up illustrating regions of interest used to quantify HER2. (F) Histogram summary showing the cutoff point for declaring cells HER2+.



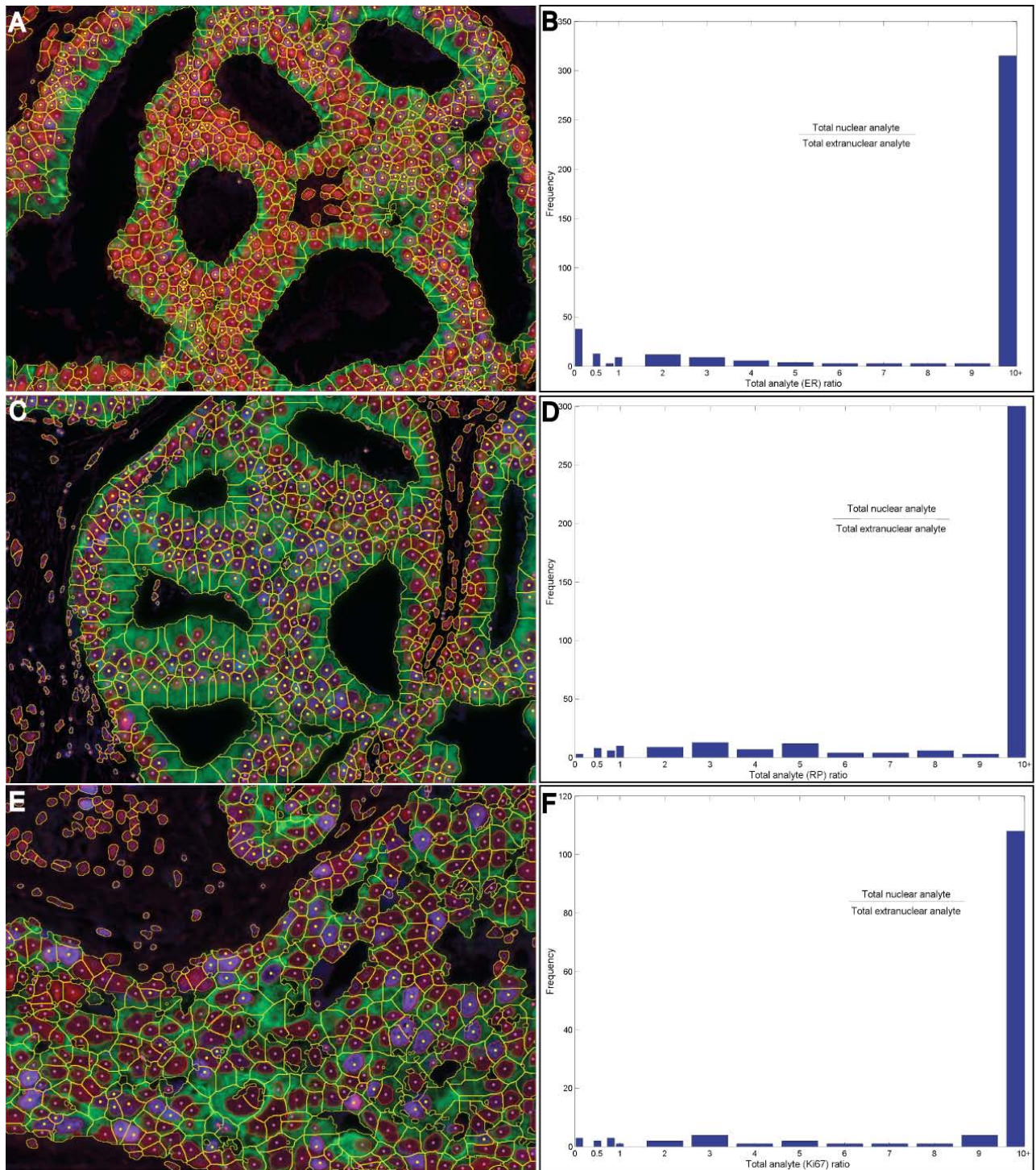


**Figure 3: Examples showing analysis of breast cancer specimens stained for three nuclear-bound biomarkers.** Breast cancer slides were immunostained for estrogen receptor (A, B), progesterone receptor (C, D), or Ki67 (E, F) plus cytokeratin and counterstained with hematoxylin. Images were captured, and nuclear and whole cell segmentation was performed, with yellow dots indicating the nuclei positive for the respective analytes (A, C, E). Analyte was quantified in the nuclear and extranuclear compartments of each cell, and histograms of the ratios of nuclear to extranuclear analyte levels in all positive cells are shown (B, D, F).

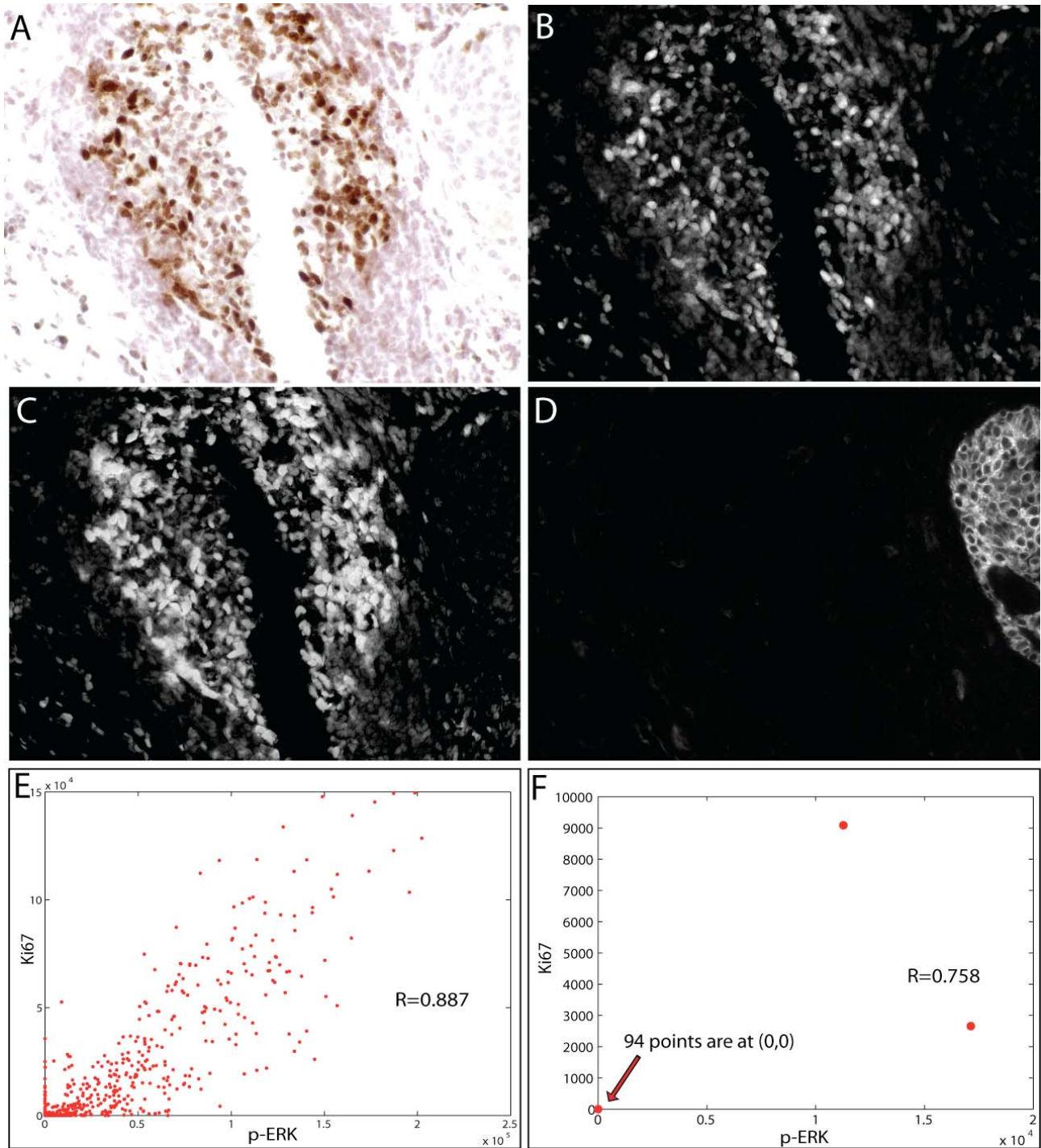


**Figure 4: Duplex analysis of pERK and Ki67 immunostaining in lymphoid cells in a human breast carcinoma.** A section of a breast tumor was stained sequentially with anti-pERK (SG blue), anti-Ki67 (DAB) and anti-CK (Alexa-488) antibodies, followed by hematoxylin staining, multispectral imaging (400X) and cytometric analysis. The brightfield image of a lymphoid nodule in the tumor is shown (A) along with the unmixed channels for DAB (Ki67) (B), SG blue (p-ERK) (C) and Alexa-488 (cytokeratin) (D). Scatter plots of p-ERK (X-axis) and Ki67 (Y-axis) staining intensity are shown for cells in the lymphoid nodule (E) and for tumor cells (F), with each dot representing one cell.



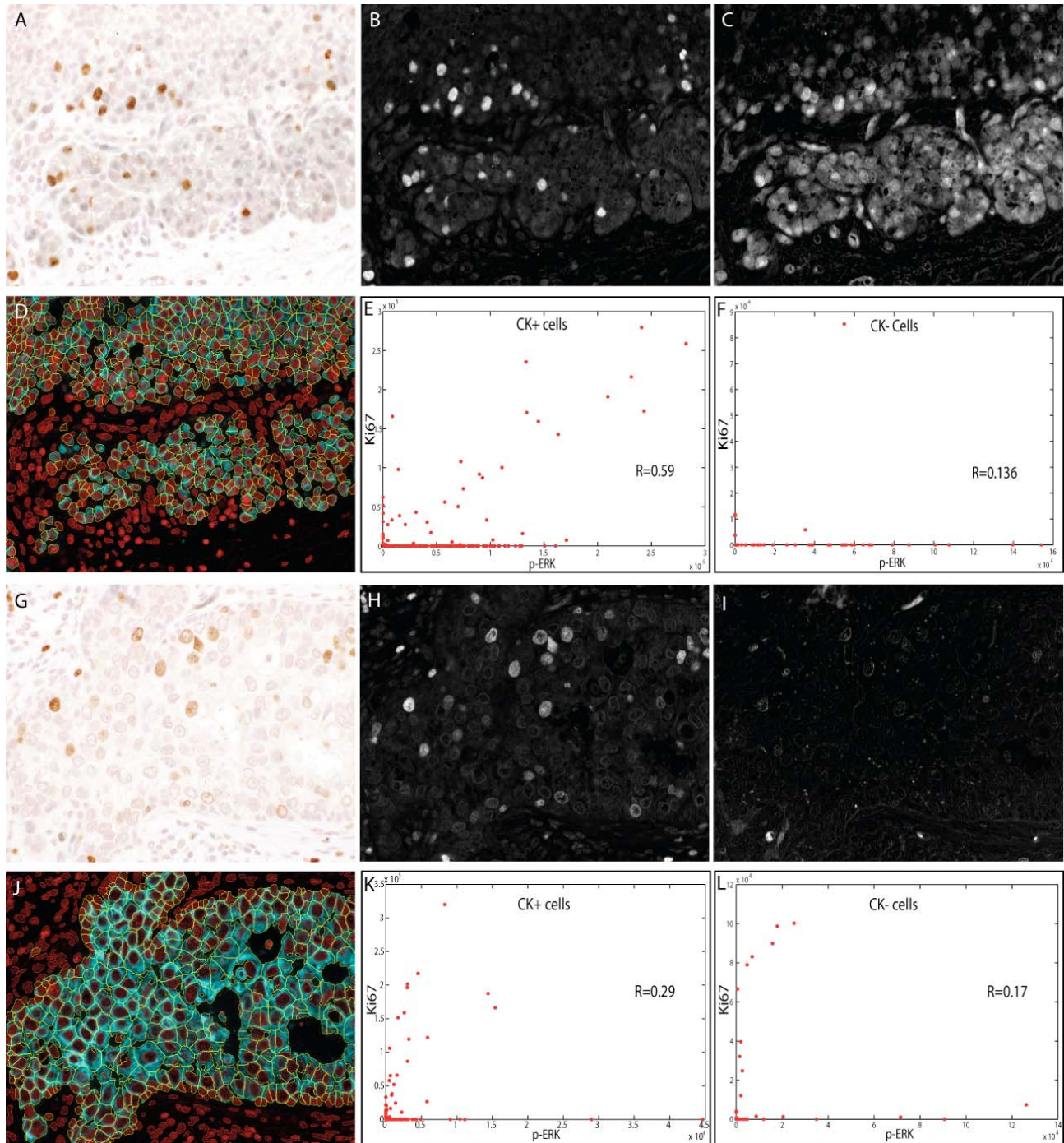


**Figure 5: Duplex analysis of pERK and Ki67 immunostaining in human breast carcinoma cells.**

Sections of two different breast tumors were stained and analyzed as described for Figure 5. Brightfield images of the two different tumors are shown (A, G), with the unmixing channels for DAB (Ki67) (B,H) and SG blue (p-ERK) (C,I). Composite images showing whole cell segmentation of the tumor (cytokeratin+) cells are shown (D,J). Scatter plots of p-ERK (X-axis) and Ki67 (Y-axis) staining intensity are shown for tumor cells (E,K) and for non-tumor (stromal) cells in (F,L) with each dot representing one cell..



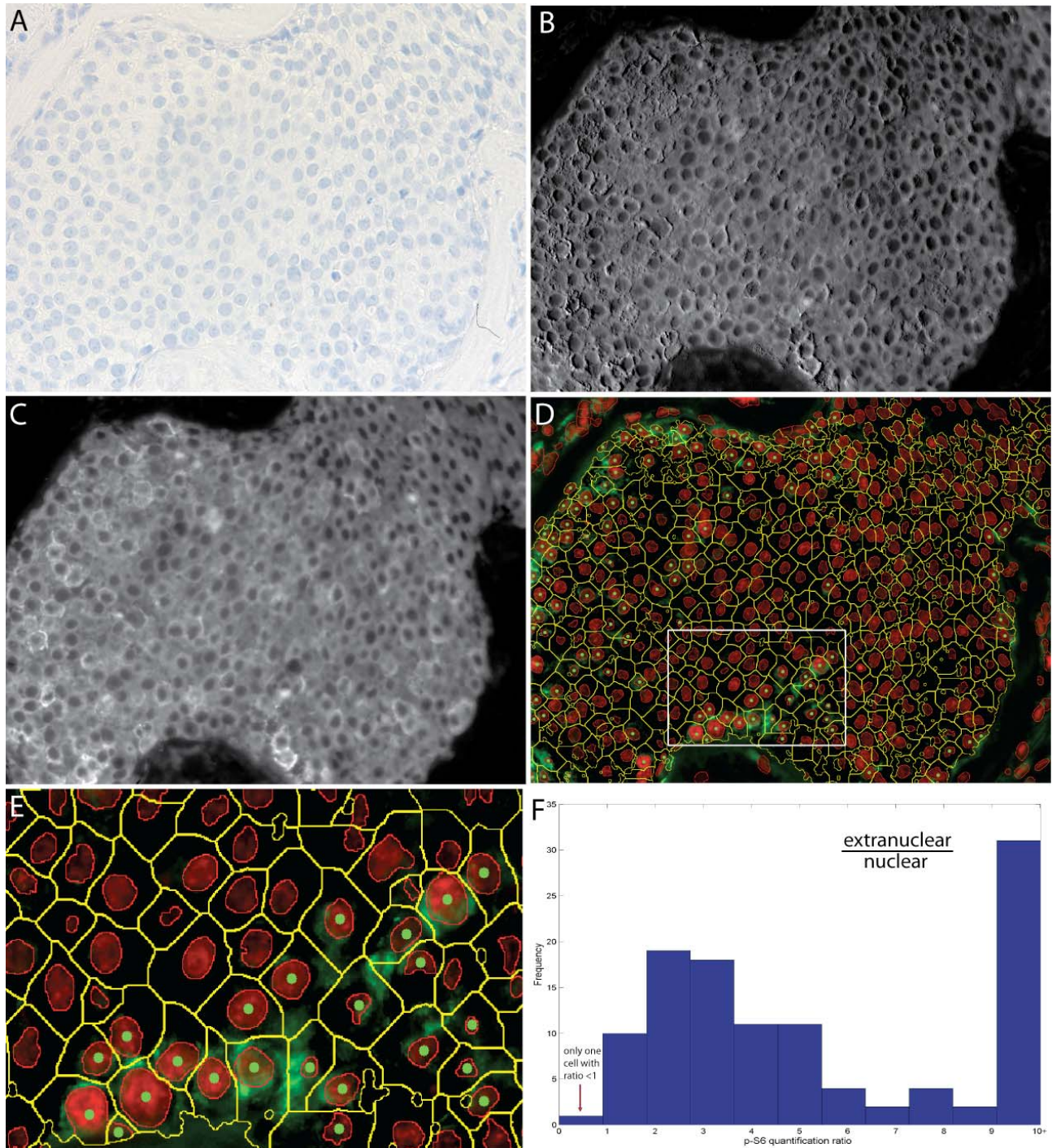
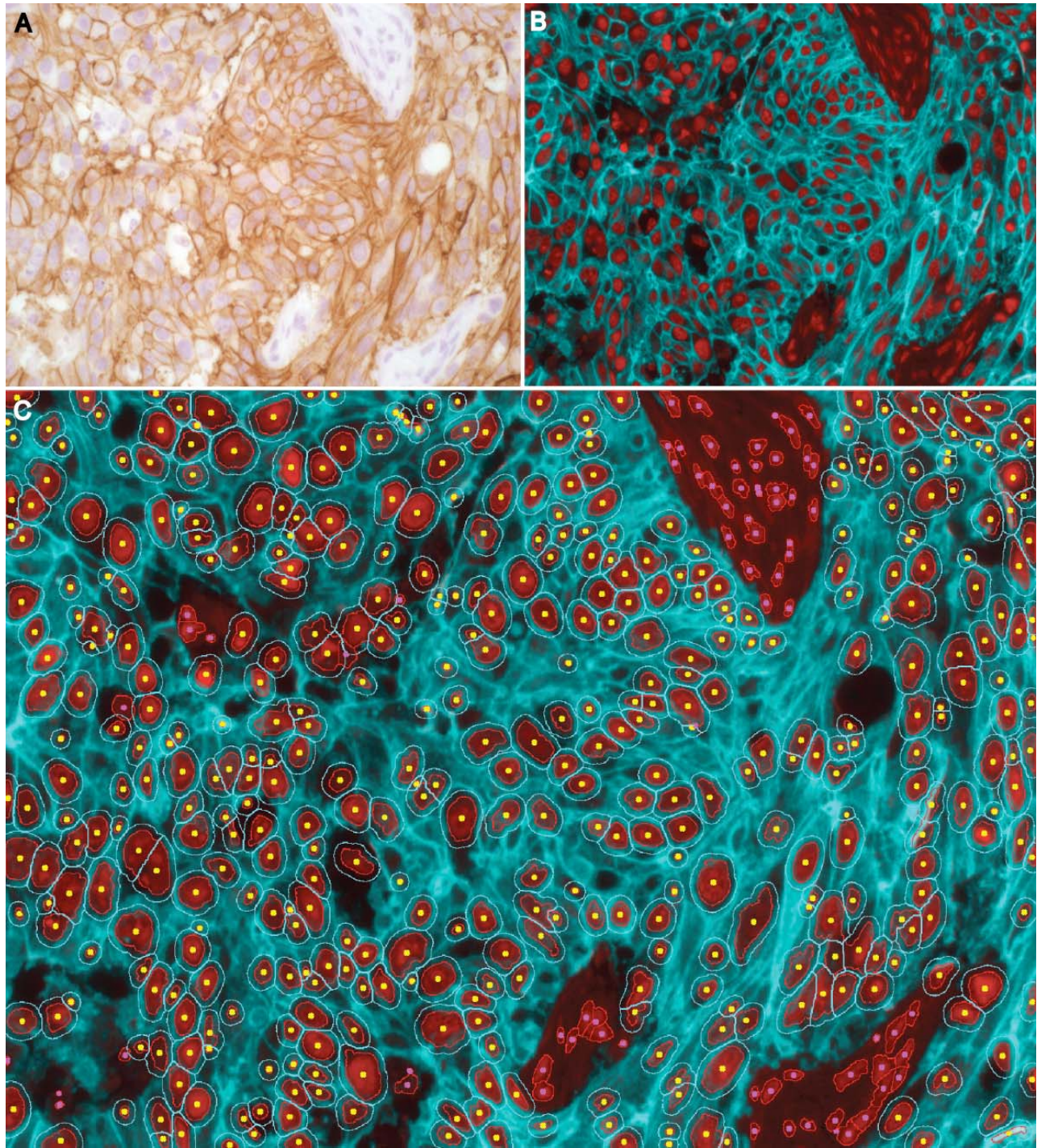


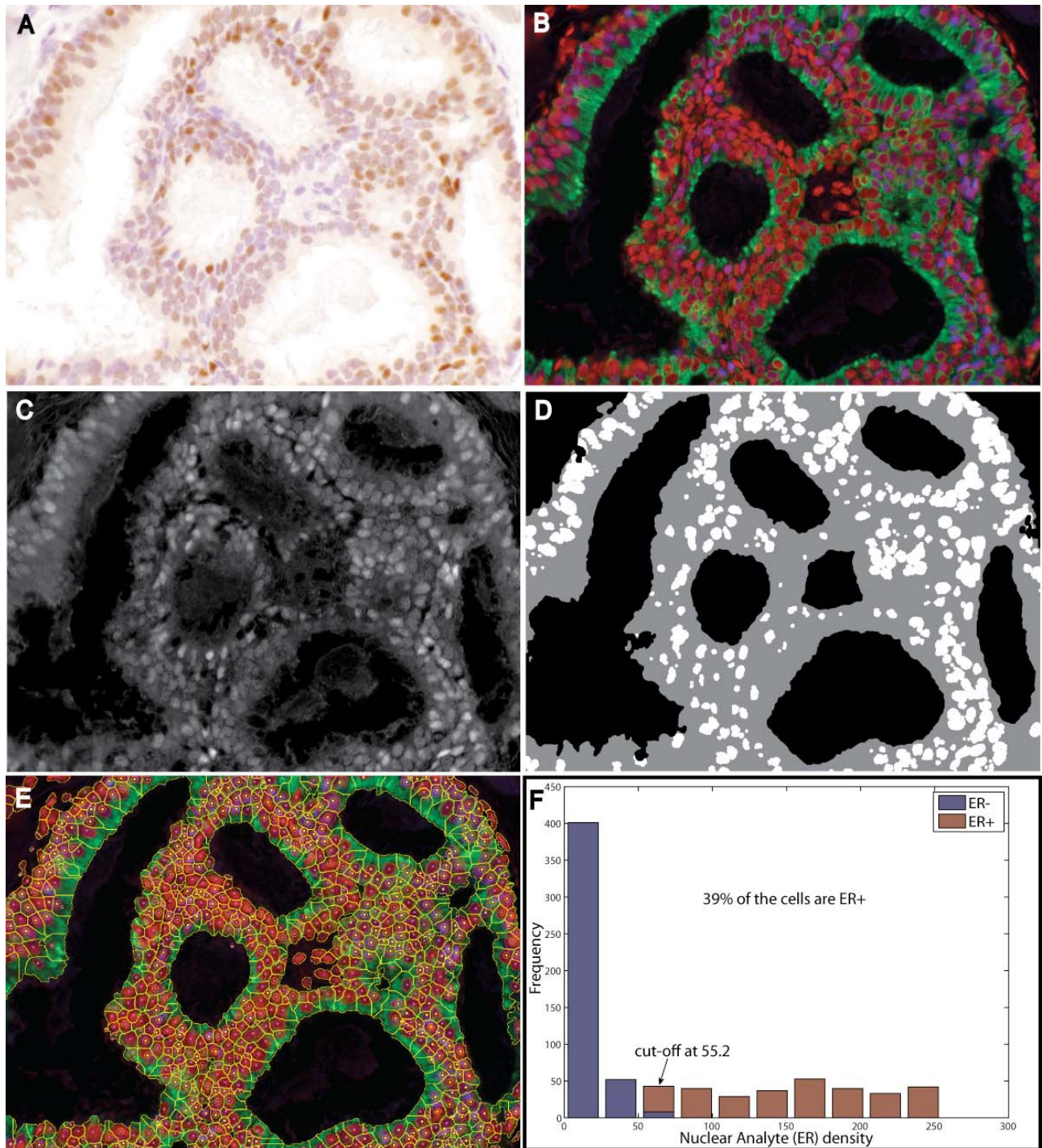
**Figure 6: Analysis of phospho-S6 immunostaining in a human breast cancer.** A section of a breast tumor was stained with anti-p-S6 (Alexa-488), anti-EMA (Alexa-594) and anti-CK (Alexa-555), followed by hematoxylin staining, multispectral imaging (400X) and cytometric analysis. The brightfield image is shown (A) along with unmixed channels for Alexa-555 (CK) (B) and Alexa-594 (EMA) (C). Composite images of p-S6 analyte staining along with segmented whole tumor cells are shown (D; E shows an enlargement of the boxed area in D). In each cell, analyte in the nuclear and extranuclear compartment was quantified. Ratios of extranuclear to nuclear analyte were calculated for each positive tumor cell and their distribution is shown (F).





**Supplementary Figure 1: Illustrating application of the proposed methods to a breast cancer specimen labeled for HER2 and cell nuclei only.** The specimen was stained for HER2 by IHC using DAB and counterstained with hematoxylin. (A) Brightfield image of slide showing HER2 staining in DAB (brown chromogen) counterstained with hematoxylin. (B) Composite 2-color image with red corresponding to the nuclear channel, and light blue corresponding to the HER2 channel. (C) Combined segmentation and classification results overlaid on the composite image shown in panel B. The bright blue outlines indicate cell boundaries that were estimated using a fixed distance of 10 pixels surrounding cell nuclei, using the method described as Case III. Yellow and pink dots represent HER2+ and HER2- cells respectively.





**Supplementary Figure 2:** Application of the proposed method to a breast cancer specimen labeled for Estrogen Receptor (ER) by IHC using DAB, and for CK by IF using Alexa-488 and counterstained with hematoxylin. (A) Brightfield image. (B) Composite 3-color image after spectral unmixing with red, green, and blue corresponding to the nuclear, cytokeratin and ER channels respectively. (C) The raw ER channel. (D) Three-level binarization of the ER channel for background correction. (E) Combined segmentation and classification results overlaid on the composite image in panel B. Yellow and pink dots indicate ER+ and ER- cells. (F) Histogram of the background-corrected intra-nuclear ER signal in cell nuclei. The ER density cut-off value between ER- and ER+ is 55.2 and 39% of the tumor cells (CK+) are identified as ER+. This percentage is very close to the manual estimate, which is 38%.

## SUPPLEMENT A: DETAILS OF IN VITRO VALIDATION EXPERIMENT

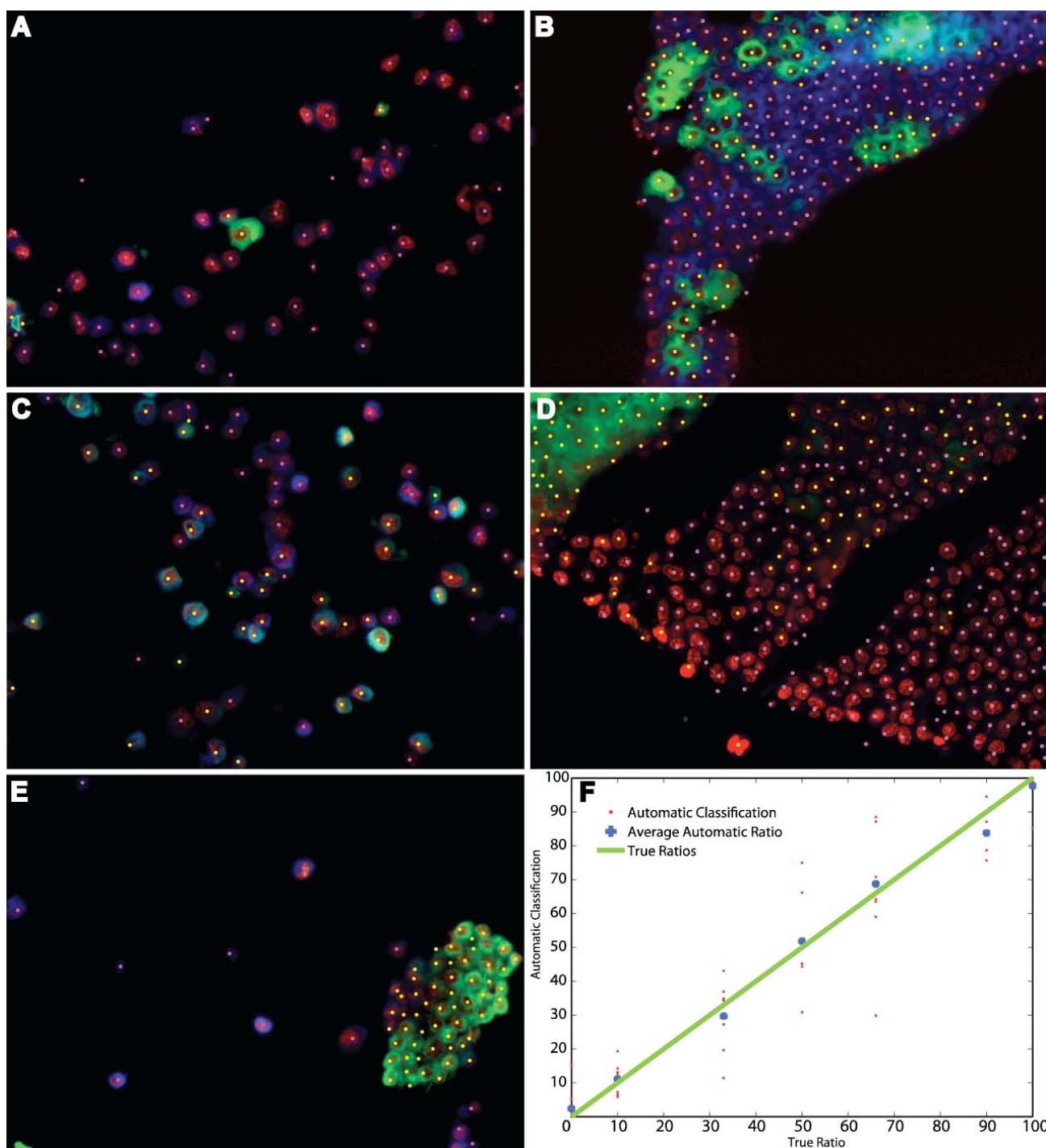
***In vitro specimens used for validation purposes:*** We specifically prepared a set of slides for the purpose of validating the performance of our integrated methodology. For this, K1735 murine melanoma tumor cells were cultured in complete media DMEM with 10% FBS and 10% penicillin/streptomycin. After trypsinization, half of the cells were labeled with plasma membrane dye PKH26 while the other half of the cells were labeled with PKH26 and PKH67 (Sigma Aldrich, Allentown, PA) according to instructions. Cells from the two labeling reactions were washed, counted and mixed together in different ratios: 0%, 10%, 33 %, 50%, 66%, 90% and 100%. Cells in the different mixtures were fixed in 2% paraformaldehyde for 2 minutes and centrifuged. The cell pellets were snap frozen in liquid nitrogen, and 10  $\mu$ M sections were cut from the frozen blocks. Sections were stained with 4', 6'-diamidino-2-phenylindole (DAPI) to reveal nuclei.

Stained slides were imaged at appropriate wavelengths to reveal nuclei, PKH26 staining and PKH67 staining (**Figure A.1**, panel A-E, respectively). Images of the pure cases (10:0, and 0:10) are not shown. In these images, the nuclear channel (DAPI) is displayed in red, the PKH26 channel is displayed in blue, and PKH67 channel in green. Ten images (400X) were taken of slides from each block and processed by FARSIGHT to segment cells and their nuclei, classify the segmented cells as PKH67-negative or PKH67-positive, and compute the ratio of the two cell populations. The intermediate image analysis steps are not shown, but only the final cell classification results are displayed by color coding the nuclear segmentation seeds. PKH26+ cells are indicated as red dots and the PKH67+ cells are shown as yellow dots. A plot of the measured proportion in every image (Y-axis) versus the true proportion of PKH67-negative cells (X-axis) is shown in panel F and demonstrates that the averages of cell proportions determined by FARSIGHT closely approximate the known truth. A comparison between the automatically found average percentages of positive cells to the corresponding ground truths for a set of sample images is provided in **Table A.1**. In interpreting these data, one must expect some natural variability from one image to the next, hence the reason for analyzing 10 images for each ratio.



**Table A.1:** *Summary of validation results comparing automated classification results against the results produced by a human expert for several of the examples shown in this paper.*

Image	Percentage of positive cells	
	Manual Average (%)	Automated Average (%)
<b>In_vitro 0%</b>	0	2.4
<b>In_vitro 10%</b>	10	11.1
<b>In_vitro 33%</b>	33	32.8
<b>In_vitro 50%</b>	50	53.7
<b>In_vitro 66%</b>	66	66.9
<b>In_vitro 90%</b>	90	86.4
<b>In_vitro 100%</b>	100	98.0
<b>In_vivo ER</b>	38	39
<b>In_vivo PR</b>	39	40
<b>In_vivo Ki67</b>	26	27
<b>In_vivo HER2</b>	99%	98.5



**Supplementary Figure A.1: Validation using *in vitro* labeled cultured cell blocks.** (A–E) Sample images of slices of “blocks” of cultured cells labeled *in vitro* with PKH26, or with a combination of PKH26 and PKH67 mixed in ratios (9:1, 2:1, 1:1, 1:2, & 1:9). Images of the pure cases (10:0, and 0:10) are not shown. The nuclear channel (DAPI) is displayed in red, the PKH26 channel is displayed in blue, and PKH67 channel in green. The final cell classification results are displayed by color-coding the nuclear segmentation seeds. PKH26+ cells are indicated as red dots and the PKH67+ cells are shown as yellow dots. (F) A plot of the measured proportion (Y-axis) versus the true proportion of PKH67-negative cells (X-axis) in every image demonstrates that the averages of cell proportions determined by FARSIGHT very closely approximate the known truth, and the absence of systematic bias.

**From:** "Badri Roysam" <roysam@ecse.rpi.edu>  
**Date:** September 8, 2010 1:20:53 PM EDT  
**To:** leemingf@mail.med.upenn.edu, yousef.kofahi@gmail.com, gramak@rpi.edu, wiem1las@yahoo.fr  
**Subject:** Fw: Histopathology - HISTOP-04-10-0247

----- Original Message -----

From: HlSedoffice@wiley.com  
To: roysam@ecse.rpi.edu, michal@rpi.edu  
Sent: Wed, 08 Sep 2010 11:54:52 -0400  
Subject: Histopathology - HISTOP-04-10-0247

08-Sep-2010

Dear Professor Roysam,

Manuscript ID HISTOP-04-10-0247 entitled "Cell-based Quantification of Molecular Biomarkers in Histopathology Specimens", which you submitted to Histopathology, has been reviewed. The comments of the reviewer(s) are included at the bottom of this e-mail.

The reviewer(s) have recommended publication, but suggest some minor revisions to your manuscript. Therefore, I invite you to respond to the reviewer(s)' comments and revise your manuscript accordingly.

To revise your manuscript, log into <http://mc.manuscriptcentral.com/histop> and enter your Author Center, where you will find your manuscript title listed under "Manuscripts with Decisions." Under "Actions," click on "Create a Revision". Your manuscript number has been appended to denote a revision.

You will be unable to make your revisions on the originally-submitted version of the manuscript. Instead, revise your manuscript using a word-processing program and save it onto your computer. Please also highlight the changes to your manuscript within the document by using the track changes mode in MS Word or by using bold or coloured text.

Once the revised manuscript is prepared, you can upload it and submit it through your Author Center.

When submitting your revised manuscript, you will be able to respond to the comments made by the reviewer(s) in the space provided. You can use this space to document any changes you make to the original manuscript. In order to expedite the processing of the revised manuscript, please be as specific as possible in your response to the reviewer(s).

**IMPORTANT:** Your original files are available to you when you upload your revised manuscript. Please delete any redundant files before completing the submission.

Because we are trying to facilitate timely publication of manuscripts submitted to Histopathology, your revised manuscript should be submitted within 30 days. If it is not possible for you to submit your revision within a reasonable amount of time, we may have to consider your paper as a new submission.

Once again, thank you for submitting your manuscript to Histopathology and I look forward to receiving your revision.

With kind regards,  
Yours sincerely,

Professor Michael Wells  
Editor in Chief, Histopathology

Reviewer(s)' Comments to Author:

Referee: 1

Comments to the Author

In the study, the authors was able to demonstrate the application of FARSIGHT software to analyze microscopic sections using spectral segmentation method, which could achieve a result similar to human expert analysis Table A.1. The method could be useful in qualification and quantification of immunohistochemistry and IF signals, and might offer more objective assessment of a test requiring quantification of an immuno-signal, like cerbB2 and grading IF in renal & skin Bx. The pictures are of good quality and are illustrative.

Some issues need to be addressed, listed as follows:

1. It appears that FARSIGHT, like most other image analysis tools, is a proprietary product and the algorithm of analysis is not known to many users.
2. Analysis using spectral segmentation requires "significant contrast" between cellular compartments and the method could not directly apply to conventional HE and many histochemical sections.
3. Much manual preparations is required in a) special staining and b) selection of image.
4. It appears that the current experimental application is concentrated with assessment of SINGLE cell type, whereas in most diseases, there will be multiple cell types that may express the same markers to a different extent.
5. How easy or feasible is this technique in assessing whole slides? Would it be too tedious?
6. How about markers showing granular staining (e.g. synaptophysin?)